Probing structural and chemical evolution in (Al$_x$Ga$_{1-x}$)$_2$O$_3$ using atom probe tomography: A review

Baishakhi Mazumder[a)], Jith Sarker

Department of Materials Design and Innovation, University at Buffalo, Buffalo, New York 14260, USA
[a)]Address all correspondence to this author. e-mail: baishakh@buffalo.edu

(Al$_x$Ga$_{1-x}$)$_2$O$_3$ is a novel ultra-wide bandgap semiconductor with the potential to dominate future power electronics industries. High-performance devices demand high Al content in (Al$_x$Ga$_{1-x}$)$_2$O$_3$ but are limited by crystallinity degradation resulting from phase separation. Additionally, the solubility limit of Al is still under debate, and conclusive research is in progress. (Al$_x$Ga$_{1-x}$)$_2$O$_3$ is also limited in high-frequency applications owing to low carrier mobility and requires n-type doping. For commercializing this material, the major obstacle is understanding dopant's behavior in the host (Al$_x$Ga$_{1-x}$)$_2$O$_3$. To investigate these issues, an advanced characterization technique, atom probe tomography (APT), was employed to analyze the structural-chemical evolution of (Al$_x$Ga$_{1-x}$)$_2$O$_3$. In this review, we summarized our recent works on the structure-chemistry investigation of (Al$_x$Ga$_{1-x}$)$_2$O$_3$ with alloy composition and doping interaction. We introduced machine learning algorithms on APT data to reveal unrivaled knowledge, previously not achievable with conventional methodologies. The outstanding capabilities of APT to study (Al$_x$Ga$_{1-x}$)$_2$O$_3$ with Al composition and doping will be considered significant for the wide bandgap semiconductors community.

Dr. Baishakhi Mazumder is an Assistant professor at the Department of Materials Design and Innovation, University at Buffalo. Dr. Mazumder received her Ph.D. in Material Science from the Université de Rouen, France in December 2010. Prior to joining University at Buffalo in 2017, she was a senior material scientist at Intel Corporation, as a research associate at Oak Ridge National Laboratory and as a post-doctoral researcher in University of California, Santa Barbara. She specializes in material analysis using advanced characterization techniques especially Atom Probe Tomography (APT). Dr. Mazumder's work in determining critical material properties using APT has contributed to the growth of next generation communication and power electronics devices. Her research interests span the areas of power electronics, optoelectronics, wide band gap semiconductors and oxide electronic materials. Her research mainly focuses on establishing processing-structure-chemistry-property-performance correlations for design and development of advanced materials.

Introduction

Over the last few decades, the comparatively low performance of conventional Si technology to meet the increasing demands for high-power, high-frequency, and high-temperature operations has led researchers to look for alternative materials with superior properties [1]. Wide bandgap semiconductors like SiC and GaN exhibited excellent properties compared with their Si counterparts; the large bandgap allowing a high breakdown field (<2 MV/cm), high saturation velocity (<2 × 10^7 cm/s), and high electron mobility (<1000 cm^2/v s) [2, 3, 4, 5, 6, 7, 8]. The

increasing demand for devices with higher breakdown and sustainability at higher temperature requires a material with even higher band gap compared with SiC (3.3 eV) and GaN (3.4 eV) [7]. Ga$_2$O$_3$, with its exceptionally higher bandgap of ~4.85 eV with a predicted breakdown field of ~8 MV/cm as well as its ability to form high-quality heterostructures [7], has gained significant attention in the power electronics industry for high-power, high-temperature applications. These properties make Ga$_2$O$_3$ ideal candidates for high-power, high-frequency switching, photodetectors, electric vehicles, and lightweight systems
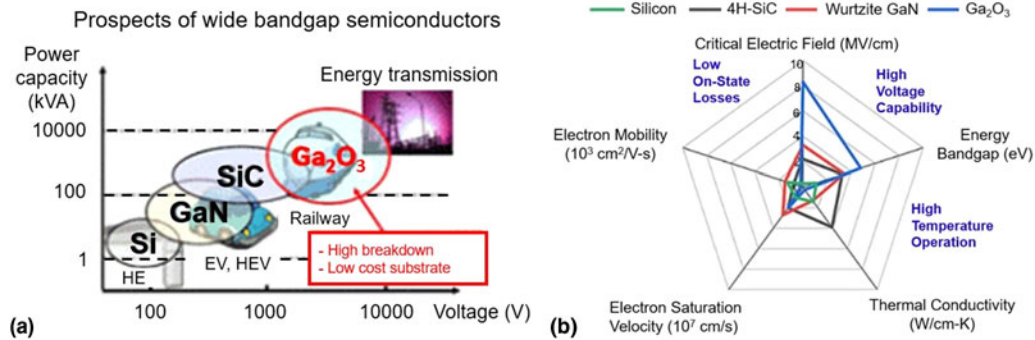
Figure 1: (a) Potential high-power applications of Ga_2O_3 based wide bandgap technology (image acquired from http://www.semiconductor-today.com/news_items/2012/JAN/NICT_160112.html); (b) pentagon showing outstanding properties of wide bandgap materials over conventional Si based technology. Reprinted with permission from Ref. [7] with the permission of AIP Publishing.

like drones, quantum information, and extreme environment applications [7, 8]. Figure 1 shows some potential applications and outstanding properties of Ga_2O_3 based materials compared with other wide bandgap semiconductors. Due to the similar electronic structure of Ga and Al with Al_2O_3 exhibiting a higher bandgap [9], it was possible to widen the bandgap of Ga_2O_3 by alloying it with Al, resulting in $(Al_xGa_{1-x})_2O_3$ with a tunable ultra-wide bandgap of 4.8 eV (β-Ga_2O_3) to 8.7 eV (α-Al_2O_3) [10] depending on Al content. $(Al_xGa_{1-x})_2O_3$ has shown unique properties including enhanced predicted breakdown strength with an improved chemical and thermal stability [10, 11], making it highly desirable for high power electronics and deep ultraviolet optical applications [9, 12]. The bandgap in $(Al_xGa_{1-x})_2O_3$ tends to increase monotonically with the incorporation of Al content [12, 13] that forms $(Al_xGa_{1-x})_2O_3$-/Ga_2O_3 heterostructures with large band offset [9]. This elevated bandgap has enabled successful realization of $(Al_xGa_{1-x})_2O_3$ based field-effect transistors [11, 14, 15, 16], Schottky barrier diodes [17, 18], and photodetectors [19, 20, 21].

As the bandgap increases with Al content [10, 12, 13, 22, 23, 24], it was expected that the device fabricated with $(Al_xGa_{1-x})_2O_3$ with high Al content would offer even higher efficiency. However, significantly degraded device efficiency was reported at high Al content beyond ~25% [20, 25]. This reduced efficiency is due to the crystallinity degradation of $(Al_xGa_{1-x})_2O_3$, arising from the solubility limit of corundum Al_2O_3 in monoclinic Ga_2O_3 beyond a certain Al content [10, 12, 26, 27, 28, 29, 30]. The theoretically predicted solubility limit of Al in $(Al_xGa_{1-x})_2O_3$ was ~60% [31, 32]. The experimental verifications of the Al inclusion range using X-ray diffraction (XRD) [26, 30], transmission electron microscopy (TEM) [23, 28], atomic force microscopy (AFM) [23, 33], and energy dispersive X-ray analysis (EDX) [26] varied over a wide range of Al content from 27% [34] to 78% [12]. The contrasting results obtained using these tools had left the solubility limit of Al in $(Al_xGa_{1-x})_2O_3$ as undetermined. A concrete conclusion could not be drawn about the Al inclusion limit

using these methods due to a lack of atomic level information on structure and composition with varying Al content. Even if the solubility limit of Al in $(Al_xGa_{1-x})_2O_3$ is experimentally verified and $(Al_xGa_{1-x})_2O_3$ with high Al content would facilitate higher device breakdown, the low carrier mobility of $(Al_xGa_{1-x})_2O_3$ would still impose a critical challenge for realizing high-frequency devices [7]. Therefore, n-type doping is necessary for these devices to perform up to their theoretical limit [35, 36, 37]. N-type doping in $(Al_xGa_{1-x})_2O_3$ is in its early stage. Although several groups confirmed dopant incorporations in $(Al_xGa_{1-x})_2O_3$ [37, 38], a detailed understanding of dopant behavior including dopant distribution with three-dimensional (3D) atomic positions within the structure, dopant segregation, and specific site occupancy is still lacking. A comprehensive study of the dopant chemistry and its influence on the electrical properties in $(Al_xGa_{1-x})_2O_3$ is required for high-performance device realization since doping in wide bandgap material has been a long-standing challenge due to self-compensation of dopants [39, 40, 41, 42, 43, 44]. Since the phase instability and difficulties in n-type doping are correlated with changes in atomic-level microstructure and chemical compositions, it is extremely important to understand the sub-atomic structural chemistry of $(Al_xGa_{1-x})_2O_3$ with varying alloy composition as well as n-type doping that requires an advanced nanoscale characterization.

The nanoscale characterization is crucial because microstructure and chemical features of semiconductors primarily dictate the localized physical and chemical entities, and therefore dictate the device efficiencies. These features include tiny precipitates or elemental segregations, impurity diffusions, interface quality, dopant profile distribution, local composition fluctuations, as well as a different form of structural or crystal defects, including lattice mismatch, grain boundaries, point defects, and dislocations [45]. The necessity and difficulty of studying these structural features has motivated the development of several high-resolution microscopic techniques such as scanning electron microscopy (SEM), scanning transmission

electron microscopy (STEM), secondary ion mass spectroscopy (SIMS), scanning capacitance microscopy (SCM), and scanning probe microscopy (SPM) [46, 47, 48, 49, 50]. Among these techniques, STEM and SIMS are standard characterization tools whose capability can be extended down to a length scale of ~100 nm [51]. STEM can provide crystallographic information with high spatial resolution and an accurate atomic-scale structure in projection [52]. However, to measure chemical compositions, it requires ancillary techniques like electron energy loss spectroscopy (EELS) or energy-dispersive X-ray spectroscopy (EDS) [52, 53]. SIMS uses a mass spectrometry approach to chemically identify the ions, thus provides more accurate compositional information compared with indirect methods (like EELS and EDS) adapted in TEM [53]. Despite improved chemical composition obtained in SIMS, the planar (x, y) positional information of individual atoms is not preserved due to uncontrolled dislodging of atoms *via* sputtering. These limitations imposed serious challenges for the existing characterization techniques in exact 3D imaging at the subatomic level, particularly when the features of interest are smaller than the specimen thickness (~10–100 nm) [54]. These conventional techniques are less developed in revealing atomic-level information such as powerful 3D mapping capability, quantification accuracy, high spatial resolutions, detecting all elements with equal sensitivity, small diffusions in buried ~1 nm interface, and in complex nanoscale or multilayer structures. Such limitations have led to the development of an advanced characterization technique, atom probe tomography (APT), to fill the information void. APT combined with field ion microscopy (FIM) and time-of-flight (TOF) spectroscopy [55] is a powerful characterization technique that enables direct 3D visualization of complex structure and chemistry at the atomic level with very high sensitivity [10 atomic parts per million (appm)] [45, 56] as well as near-atomic spatial and chemical resolution [57]. Over the last decade, APT has been widely used to study the atomic-level structural chemistry including local elemental segregation/clustering, layer homogeneity, interface RMS roughness, adatoms diffusions across the interfaces in wide bandgap semiconductors, and their heterostructures to explain local chemical and physical properties that directly manipulate the corresponding electrical/optical devices [18, 58, 59, 60, 61, 62, 63, 64, 65, 66, 67, 68, 69]. In addition to all these capabilities, atom collection in APT experiments provides their position coordinates, TOF, and mass-to-charge states (m/q) of each atom [57]. These parameters can be trained *via* advanced data mining (unsupervised machine learning algorithms) to extract patterns in APT data to predict additional material features such as phase information [70], isotope discrimination [71], crystallographic orientations [72], and automated cluster detection and identifying uncertainty in user-defined precipitates/clustering [73].

Recently, we have published a series of papers on the atomic-scale structure-chemistry analysis of $(Al_xGa_{1-x})_2O_3$ using APT. We demonstrated how APT along with advanced statistical analysis tools can reveal the material information that are critical for design of new ultra-wide bandgap materials for future power electronics applications. In this article, we present a comprehensive review on the recent progress of the advanced characterization of $(Al_xGa_{1-x})_2O_3$ using APT that provides direct insight on the atomic-level evolution of $(Al_xGa_{1-x})_2O_3$ films with varying alloy composition. How the change in Al content in $(Al_xGa_{1-x})_2O_3$ affects the subsequent chemical and physical properties is reviewed. The adaptation of advanced machine learning on APT data was emphasized to predict phase transformations in this alloy without any supporting characterization tools. The detection, quantification, and distribution of n-type dopants in $(Al_xGa_{1-x})_2O_3$ crystals were demonstrated. Moreover, the capability of APT to assess the nearest-neighbor distribution of n-type dopants in $(Al_xGa_{1-x})_2O_3$ provides a new insight to the doping interaction in this material.

Experiments

To obtain a rich data set in the APT experiment that would reveal significant information about the atomic-level structure and compositions of the materials, certain procedure is followed from preparing the needle-shaped specimen from any given bulk wafer till advanced data analysis. Similar to different materials, ranging from metals to semiconductors, atom probe experiments for wide bandgap $(Al_xGa_{1-x})_2O_3$ were carried out in three steps: (i) needle-shaped specimen preparation, (ii) data acquisition, and (iii) tip reconstruction and subsequent data analysis [74, 75, 76, 77]. In the following sub-sections, we will provide a brief description of each step.

Specimen preparation

Specimen preparation is the most critical step in APT since the field evaporation of atoms by directly probing the surface of a bulk wafer is not feasible [78]. The field evaporation and collection of atoms requires the application of a very large electric field (20–40 V/nm) to the sample [79]. These fields can only be achieved by geometric field enhancement. This field was realized by preparing the specimen apex with a radius of curvature of 50–100 nm for a wide range of materials. Also, the applied field interacts not only with the sharpened tip but also with other features within reasonable proximity (several mm) of the sharpened tip. Therefore, maintaining the electric field required for evaporation requires long, sharp needle-shaped specimens with no material in proximity of the tip [79]. The requirement for most of the APT specimen is similar

Invited Feature Paper – Review

to a certain degree for all the material system: (i) the specimen should be sharp with an end radius of ~100 nm to allow field evaporation, (ii) it should be mechanically robust to sustain the evaporation process under high electric field, and (iii) the feature or region of interest must be in the near apex region of the tip so that it lies within the collection of evaporated ions (before the premature rupture of specimen or experiment is aborted) [80]. Premature specimen fracture is likely to occur in heterostructure samples as the voltage-induced stress is more likely to exceed the mechanical stability of the tip, especially while passing through the interfaces [81, 82]. Focused ion beam (FIB)-based lift-out and annular milling was performed as outlined by Larson et al. [57, 75, 83, 84] for sample preparation. This method is most widely used for APT specimen preparation, especially, when multilayer semiconductor materials are involved [85]. Prior to the APT specimen preparation, a Ni cap layer of ~50 nm was deposited over all the $(Al_xGa_{1-x})_2O_3$ films to protect them from Ga induced surface damages and contaminations. The steps of the site-specific specimen preparation are illustrated in Fig. 2. Trenches were milled in three sides around the area of interest protected by Pt capping as shown in Fig. 2(a). The wedge was removed from the wafer by attaching a micromanipulator to the already cut and free left end of the wedge with subsequent cutting of the wedge from the right end that was attached to the bulk wafer as illustrated in Fig. 2(b). The lifted-out wedge was adjoined on a Si

Figure 2: Methodologies of APT specimen preparation from the bulk substrate to final needle-shaped $(Al_xGa_{1-x})_2O_3$ films step by step using FIB-based nanofabrication.

micro-post by Pt deposition as shown in Fig. 2(c). The wedge is then cut free from the micro-post by ion beam milling [Fig. 2(d)], and rest of the wedge attached to the micromanipulator was transferred to other empty Si posts. Pt was deposited on the opposite sides of the wedge-Si post interfaces [Fig. 2(e)]. Sharpening of the mounted post was performed by annular milling followed by 2 kV Ga ion beam cleaning resulting in the needle-shaped APT specimen as shown in Fig. 2(f). Most of the protective Ni cap layers that were deposited before starting the specimen preparations were removed during the 2 kV sharpening process, and only ~5 nm of the Ni layer at the top of the needle was left intentionally. This remaining Ni layer provided the time required for the optimization of the APT experiment condition prior to the acquisition of ions from the $(Al_xGa_{1-x})_2O_3$ layers begin. These protective Ni layers were excluded during the 3D atomic reconstructions (the "3D atomic reconstruction of the original specimen and subsequent data analysis" section) and data analysis (the "Results section").

Data acquisition

The data acquisition from the specimens is conducted by the field evaporation of ions from the specimen surface [70]. Figure 3 shows a schematic of the operating principle of APT. In the data acquisition stage, the atoms are sequentially extracted from the needle-shaped surface by controlled field evaporation. This field evaporation is initiated by first ionizing the surface atoms under an intense electrostatic field and then emitting the ions from the tip apex by applying ultrafast laser pulses (355 nm wavelength ultraviolet laser equipped in a CAMECA LEAP 5000 XR atom probe system [86]). Since wide bandgap semiconductor tips may exhibit poor response to laser pulsing, it is critical to optimize the APT experimental conditions, especially the base specimen temperature and pulse energy beforehand [80]. Experimental parameters including temperature (K), pulse repetition rate (kHz), laser pulse energy (pJ), and evaporation rate (ions per pulse) were optimized to ensure efficient data acquisition from $(Al_xGa_{1-x})_2O_3$ tips containing layered structure with varying Al content [28, 29, 87, 88]. The evaporated ions from individual layers are projected and collected in a position-sensitive detector (PSD) that provides the TOF and detection event in 2D positions [89] which is used in the reconstruction of the 3D tip image and data analysis.

3D atomic reconstruction of the original specimen and subsequent data analysis

CAMECA's Integrated Visualization and Analysis Software (IVAS 3.8.5a34) was used for the tip reconstruction of the collected APT data. The TOF of all collected ions is transformed
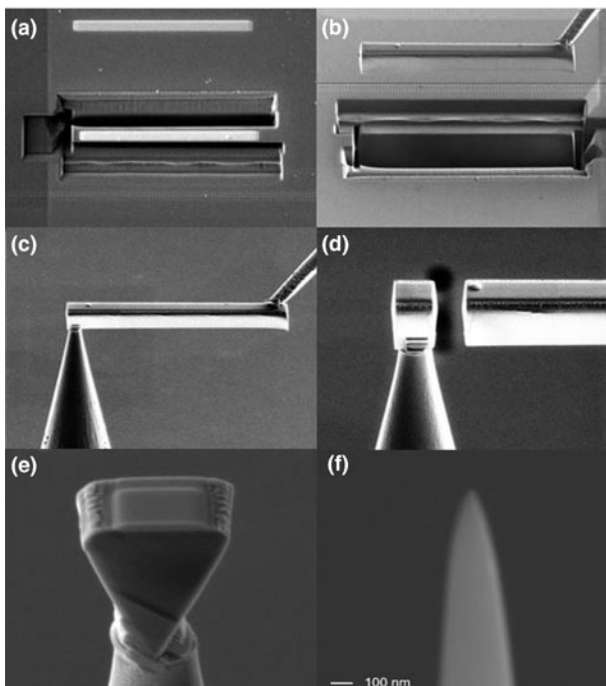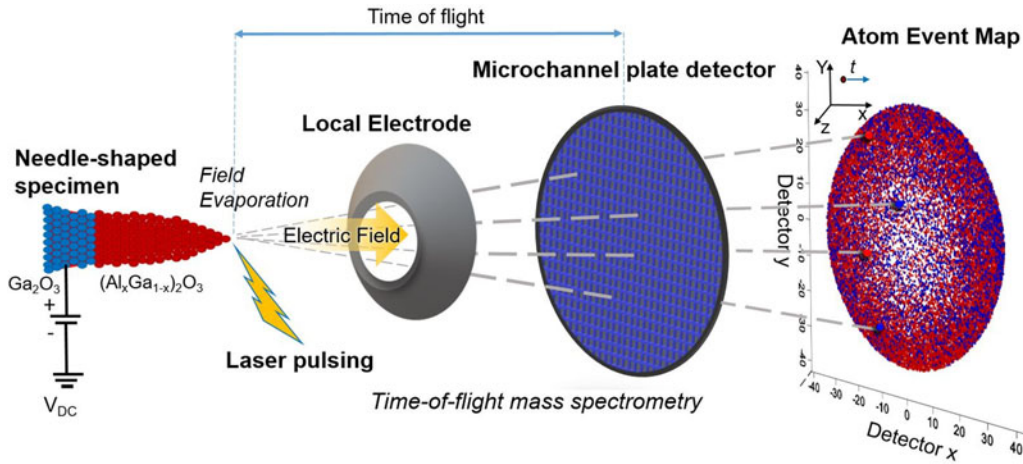
Figure 3: Schematic presentation of APT operating principle; the field evaporated atoms from the specimen surface by laser pulsing are collected on PSD. PSD records the TOF and position of impact for each and every detected atom.

into the mass-to-charge state ratio (m/n) which resolves into the mass spectrum [57]. The quality and accuracy of the data is enhanced by background correction of the mass spectrum [57, 89]. The 3D atom maps of the probed regions were reconstructed in IVAS by following the tip profile method from high magnification SEM images of the tips [57]. IVAS and MATLAB were used for data analysis (structural chemistry of $(Al_xGa_{1−x})_2O_3$ films). Due to large amount of ions collected in APT, some material features are suppressed or remain as "concealed" within the massive data set [71]. The advanced data mining strategy was employed to train unprocessed APT data and extract hidden patterns in data to predict material properties such as phase transformation.
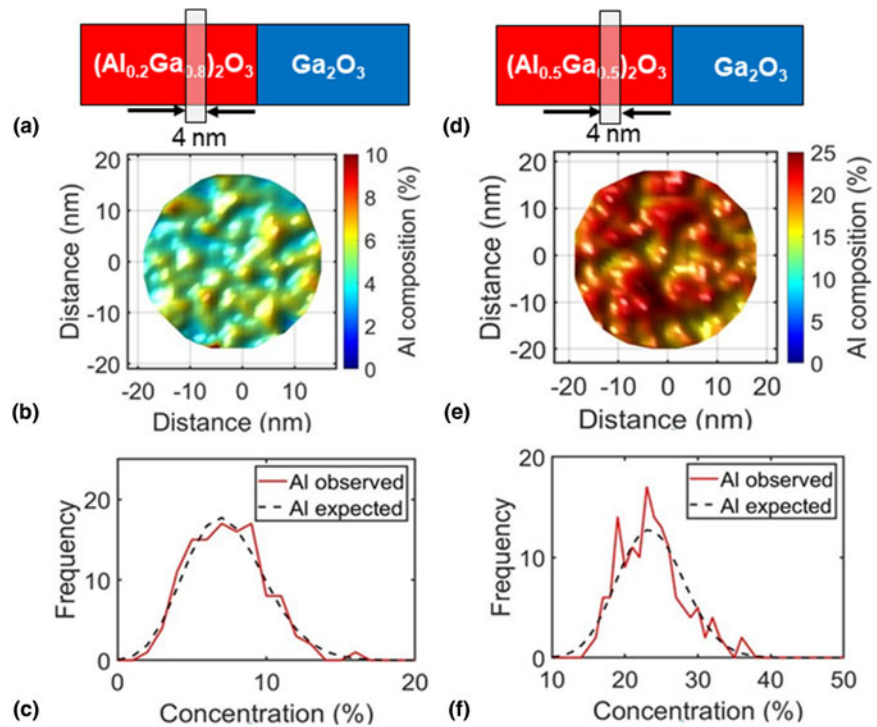
Results

Phase transformations of $(Al_xGa_{1−x})_2O_3$

The change in the atomic-level structure and chemical composition of $(Al_xGa_{1−x})_2O_3$ at Al content, $x > 0.25$, results in a degraded crystallinity of the films [28, 29, 87, 88] limiting the solubility of α-Al_2O_3 in β-Ga_2O_3. This crystal degradation was attributed to the phase separations in $(Al_xGa_{1−x})_2O_3$ at high Al content [10, 26, 28, 29, 30]. Since the phase purity is related to film's homogeneity with well-defined Al/Ga stoichiometry at the atomic level, it is required to study the change in the atomic-level structure and chemistry of $(Al_xGa_{1−x})_2O_3$ with Al to conclusively determine the Al solubility limit in this alloy. Theoretical studies suggested that elemental segregations are introduced within alloys during phase transformations [90, 91]. APT is capable of providing information about such phase transformations by mapping atomic-scale compositional variations within the materials by revealing the presence of local segregations or inhomogeneity associated with different chemical phases [92, 93, 94]. Very recently, APT was employed

to investigate the corresponding change of the atomic-level structural chemistry of $(Al_xGa_{1−x})_2O_3$ with Al content to observe phase transformation of this alloy [87, 88].

Two different $(Al_xGa_{1−x})_2O_3$ structures with Al content, $x = 0.20$ and 0.50, were investigated for comparing their structural chemistry. The details of the materials' structures are reported in Ref. [87]. A volume of $50\ nm \times 50\ nm \times 4\ nm$ region was extracted from the bulk region of both $(Al_{0.20}Ga_{0.80})_2O_3$ and $(Al_{0.50}Ga_{0.50})_2O_3$ films to investigate the homogeneity of the films in terms of elemental distribution as shown in Figs. 4(a) and 4(d), respectively. Figure 4(b) depicts the local Al distribution along the lateral XY plane in the $(Al_{0.20}Ga_{0.80})_2O_3$ films. Almost homogeneous Al distribution is observed with only 1–2 at.% fluctuations in Al composition. No significant Al segregation was observed, suggesting desired stoichiometry was maintained. The film homogeneity was confirmed *via* the statistical frequency distribution analysis (FDA) method as shown in Fig. 4(c). In FDA, if the observed elemental distribution resembles with a binomial fitting, this would suggest a homogeneous elemental distribution, while the deviation of the observed distribution from the binomial fitting would indicate statistically significant elemental segregations [94]. For $(Al_{0.20}Ga_{0.80})_2O_3$ films, the observed frequency count of Al is fitting with the random binomial distribution, suggesting homogeneous $(Al_xGa_{1−x})_2O_3$ layers. A similar compositional analysis was performed in the bulk region of the $(Al_{0.5}Ga_{0.5})_2O_3$ layer. The lateral Al distribution shows severe fluctuations of 10–12 at.% in Al composition identified by the Al-segregated regions (~25 at.% Al) and Al-depleted (~15 at.%) regions as shown in Fig. 4(e). The subsequent FDA analysis of Al distribution in Fig. 4(f) shows a significant deviation from the randomness, suggesting the inhomogeneous $(Al_{0.5}Ga_{0.5})_2O_3$ layer. The reported Pearson coefficient (μ) was 0.8 with a *P*-value of <0.0001. This high Pearson coefficient

Figure 4: (a) Schematic of the $(Al_{0.2}Ga_{0.8})_2O_3/Ga_2O_3$ structure with a black box region showing the volume extracted for analysis, (b) lateral Al distribution within the bulk of the $(Al_{0.2}Ga_{0.8})_2O_3$ layer, (c) FDA analysis of Al distribution in $(Al_{0.2}Ga_{0.8})_2O_3$ (Pearson coefficient, $\mu = 0.1$, P-value = 0.2), (d) schematic of the $(Al_{0.5}Ga_{0.5})_2O_3/Ga_2O_3$ structure with a black box region showing the volume extracted for analysis, (e) lateral Al distribution within the bulk of the $(Al_{0.5}Ga_{0.5})_2O_3$ layer, and (f) FDA analysis of Al distribution in $(Al_{0.5}Ga_{0.5})_2O_3$ (Pearson coefficient, $\mu = 0.8$, P-value <0.001). Reprinted with permission from Ref. [87] with the permission of AIP Publishing.

with low P-value confirms that a statistically significant amount of segregation is present in the layer with a 95% confidence level during the null hypothesis testing. These results indicate that, at high Al content ($x = 0.50$), the film homogeneity and stoichiometry are not maintained.

This stoichiometric deviation at high Al content was inferred to appear from the presence of different chemical phases. This was confirmed by comparing APT results with TEM and nano-diffraction patterns as shown in Fig. 5. Figure 5(a) shows the lateral distribution of Al/Ga ratio. Existence of Al-rich and Ga-rich regions are observed throughout the plane resulting from the deviations in expected 50:50 ratios of Al and Ga. These Al-rich and Al-depleted regions imply different chemical phases in the $(Al_{0.5}Ga_{0.5})_2O_3$ layers. The variation in chemical phases was confirmed by high-angle annular dark-field scanning electron microscopy (HAADF STEM) imaging of the $(Al_{0.5}Ga_{0.5})_2O_3/\beta$-$Ga_2O_3$ structure as shown in Fig. 5(b). The (010) β-Ga_2O_3 substrate shows uniform color contrast, suggesting the homogeneous layer while a contrast variation is observed in $(Al_{0.5}Ga_{0.5})_2O_3$ resulting from chemical segregation (inhomogeneity) in this layer. This indicates the presence of different chemical phases within the $(Al_{0.5}Ga_{0.5})_2O_3$ layer. Phase segregation of this $(Al_{0.5}Ga_{0.5})_2O_3$ film was studied by the nano-diffraction pattern with respect to the (010) β-Ga_2O_3 substrate. The nano-diffraction pattern of the pure monoclinic β-Ga_2O_3 substrate is shown in Fig. 5 (c). The nano-diffraction pattern for $(Al_{0.5}Ga_{0.5})_2O_3$ in Fig. 5 (d) displays additional spots which were not present in pure

monoclinic β-Ga_2O_3 in Fig. 5(c). This suggests that an additional phase is present in $(Al_{0.5}Ga_{0.5})_2O_3$ which can be correlated to the chemical segregations observed in this layer. This study reveals that chemical heterogeneity observed in APT can be attributed to phase segregations in wide bandgap alloys. Such compositional heterogeneity that leads to the phase segregations in $(Al_xGa_{1-x})_2O_3$ may be attributed to the different surface mobilities of Al and Ga adatoms [87]. Ga atoms with higher adatom mobility can easily drift and are distributed uniformly on the surface, while Al atoms with low surface mobility tend to develop segregated regions that potentially contribute to the observed compositional fluctuations [87, 88].

Since APT is capable of providing the most accurate information about phase transformations with varying alloy content, a systematic study was conducted to determine the phase transformations in $(Al_xGa_{1-x})_2O_3$ for a wide Al content range of $x = 0.1$–1.0 [28]. The analyzed structures are depicted in Fig. 6, and details about this structure is reported in Ref. [38]. Figure 6(a) shows the schematic of the $(Al_xGa_{1-x})_2O_3$ layered heterostructure grown on β-Ga_2O_3 substrates where Al composition was varied from 10 to 100% with a thickness of 20 nm for each layer. Figure 6(b) shows the Al/Ga ratio along the growth showing the stoichiometry was maintained and the grown $(Al_xGa_{1-x})_2O_3$ is ideal for studying the phase transformation.

Figure 7(a) shows the reconstructed 3D atom map with red and blue dots representing Al and Ga atoms, respectively. The change in the density of red and blue dots indicates the change
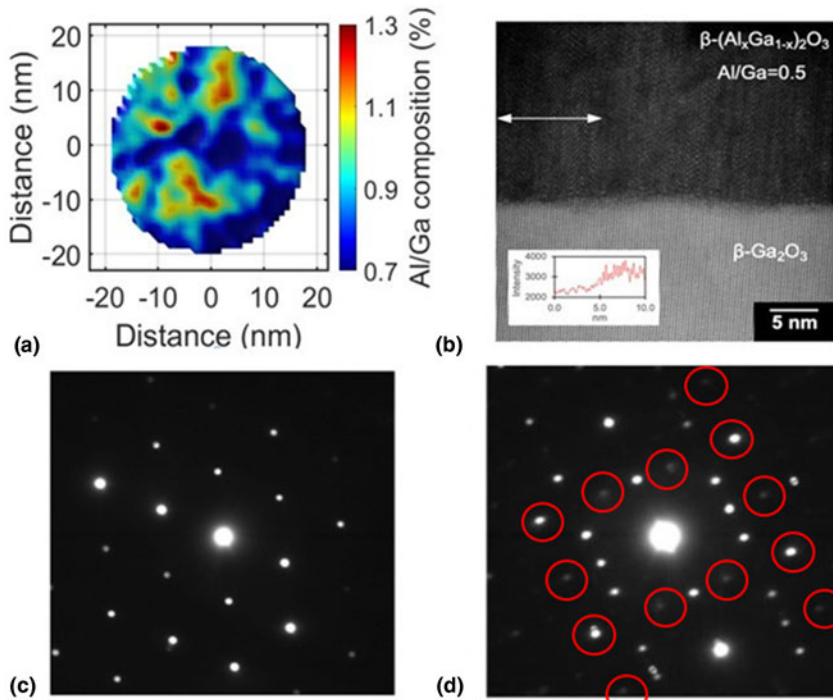
Figure 5: (a) Al/Ga composition ratio in bulk $(Al_{0.5}Ga_{0.5})_2O_3$ films and (b) HAADF STEM image of the $(Al_{0.5}Ga_{0.5})_2O_3/\beta$-$Ga_2O_3$ structure, the intensity line profile across the white arrow (inset). Nano-diffraction patterns (probe size = 1 nm) from (c) β-Ga_2O_3 and (d) $(Al_{0.5}Ga_{0.5})_2O_3$ shown in (b). Reprinted with permission from Ref. [87] with the permission of AIP Publishing.
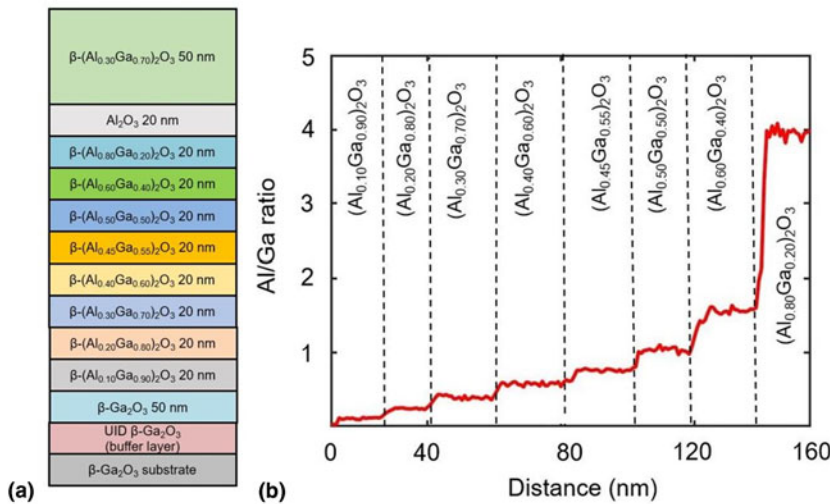

Figure 6: (a) Schematic diagram of the $(Al_xGa_{1-x})_2O_3$ heterostructure with Al content $x = 0.10–1.0$ and (b) Al/Ga ratio along the growth showing precisely controlled stoichiometry [29].

in alloy chemistry along the growth. Due to the large number of ions collected, it is difficult to discriminate each $(Al_xGa_{1-x})_2O_3$ layer with different Al composition. The lateral chemistry in each layer was investigated by plotting the lateral Al/O ratio as shown in Figs. 7(b)–7(j). For this, 4-nm-thick volumes from the bulk region of each $(Al_xGa_{1-x})_2O_3$ layers were extracted to eliminate interfacial effects (adatoms diffusion from top or bottom layers) as explained in Fig. 7(a). At low Al content ($x = 10–20\%$), a nearly homogeneous distribution was observed as shown in Figs. 7(b) and 7(c). This elemental homogeneity is an indication of single-phase stable crystalline $(Al_xGa_{1-x})_2O_3$ films. Within this Al content range, the

$(Al_xGa_{1-x})_2O_3$ films are single monoclinic β-phase stable [10, 12, 23, 26, 30, 33, 95, 96]. As the Al content increases, severely Al-segregated regions appear, as shown in Figs. 7(d)–7(g), suggesting degraded crystallinity due to the co-existence of different chemical phases of $(Al_xGa_{1-x})_2O_3$ films within this Al content range. When the Al content is even higher ($x = 0.60–1.0$), the elemental heterogeneity starts decreasing and homogeneous Al/O distribution is observed as illustrated in Figs. 7(h)–7(j). This regained homogeneity in Al/O distribution with increasing Al content is an indication of the formation of new crystalline α, γ, or η-phase [10, 26, 27, 28]. The corresponding FDA plots (with bin size = 300 atoms) for Al
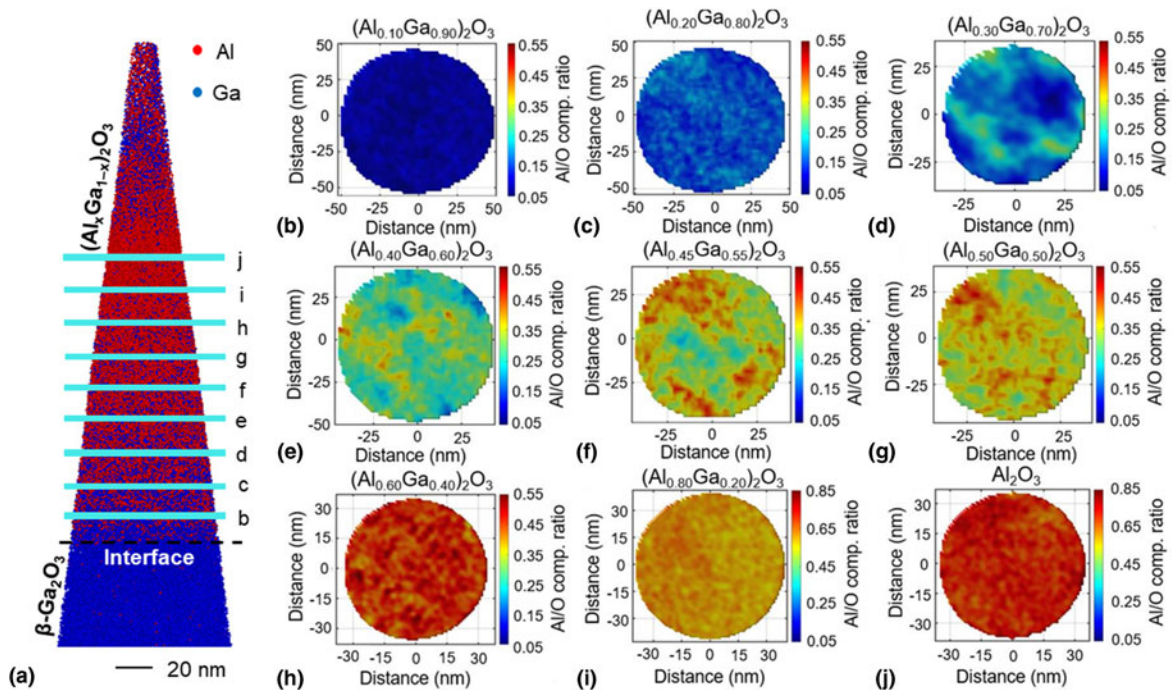
Figure 7: (a) Reconstructed atom map of the $(Al_xGa_{1-x})_2O_3$ layered heterostructure with Al composition varying from $x = 10$–100%, only Al and Ga atoms are shown by red and blue dots, respectively; Lateral distribution Al/O concentration ratio in each layer with the Al composition of (b) $x = 0.10$, (c) $x = 0.20$, (d) $x = 0.30$, (e) $x = 0.40$, (f) $x = 0.45$, (g) $x = 0.50$, (h) $x = 0.60$, (i) $x = 0.80$, and (j) $x = 1.0$. Reprinted with permission from Ref. [29] with the permission of AIP Publishing.

distribution to statistically quantify the layer's homogeneity are shown in Fig. 8. From the FDA results, it is obvious that, at low Al content of $x = 0.10$–0.20, the observed Al distribution almost aligns with the random binomial fitting with low value of Pearson coefficient (μ). This suggests homogeneous Al distribution in these layers. The FDA for layers with $x = 0.30$–0.50
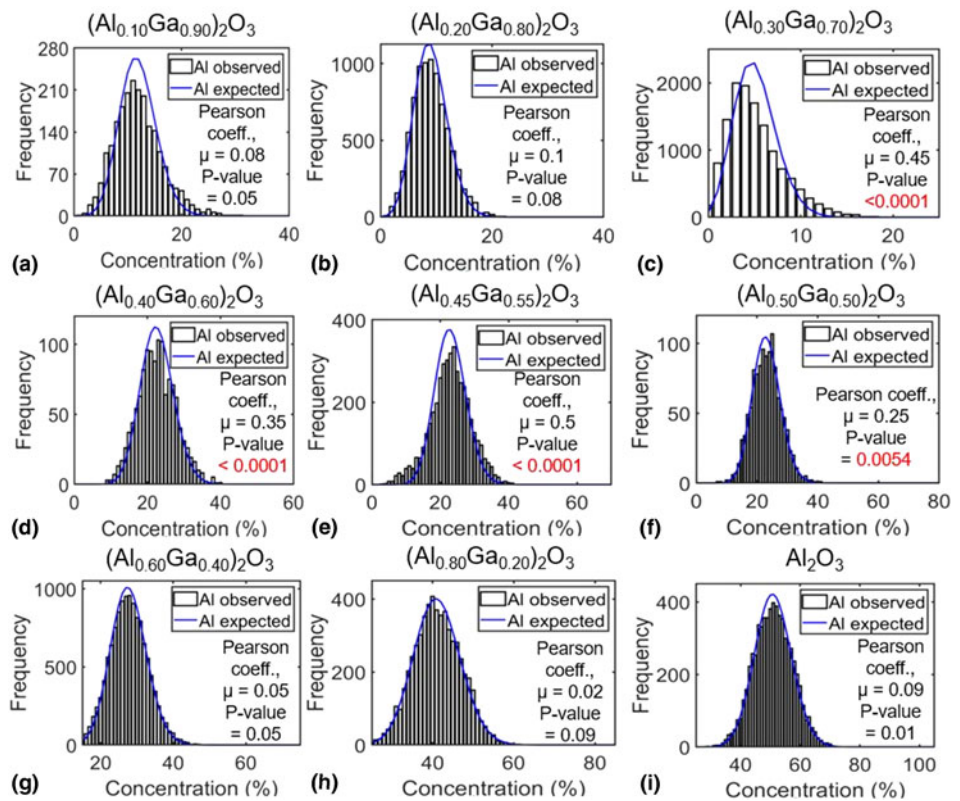

Figure 8: FDA of each layer with Al concentration: (a) $x = 0.10$, (b) $x = 0.20$, (c) $x = 0.30$, (d) $x = 0.40$, (e) $x = 0.45$, (f) $x = 0.50$, (g) $x = 0.60$, (h) $x = 0.80$, and (i) $x = 1.0$ [28].

demonstrates the extent of deviations in observed Al distribution from the binomial fitting with high value of Pearson coefficient. This confirms statistically significant elemental segregation within these layers indicating degraded crystallinity resulting from different chemical phases. However, when the Al content increases further ($x = 0.60$–1.0), the observed Al distribution coincides with that of the binomial distribution followed by low values of Pearson coefficient. This suggests that homogeneous Al distribution throughout the lateral planes is achieved again indicating regained crystallinity. XRD was performed to identify the phases present in the $(Al_xGa_{1-x})_2O_3$ films with different Al compositions [28]. The XRD peaks were identified as β-phase stable $(Al_xGa_{1-x})_2O_3$ films at low Al content ($x = 0.10$–0.20), while the XRD peaks were attributed to γ-phase $(Al_xGa_{1-x})_2O_3$ at high Al contents ($x > 0.50$) with the co-existence of mixed (β+γ)-phase when the Al content, x is in between ($x = 0.20$–0.50).

Machine learning in APT to study phase transformation of $(Al_xGa_{1-x})_2O_3$

Supporting characterization tools (STEM, nano-diffraction, and XRD) were required to confirm if the $(Al_xGa_{1-x})_2O_3$ film inhomogeneity or elemental (Al) segregation revealed by APT were indicative of phase transformations due to varying Al content. The reason is, some material features (phase transition for example) remain as "latent" within the huge amount of data (ions) collected in APT [71, 97]. Very recently, an unsupervised machine learning approach, principal component analysis (PCA), has been applied to APT data to enable the extraction of patterns from the unprocessed data set to capture material's phase-related information, which usually remains as hidden due to high dimensionality of the data [29]. PCA reduces the data dimensionality by transforming multi-component quantities of directionally correlated variable sets into a linearly uncorrelated variable set and still preserving most of the information [97]. These transformed linearly uncorrelated variable sets are the principal components (PCs) in the dimensionally reduced data set. PCA generates principal alignment directions on the basis of how much variance in the data is captured. The variance of material features such as alloy composition variation captured by these PCs is interpreted and correlated to the corresponding material properties like phase transitions [98]. In PCA analysis, principal component 1 (or PC1) represents the direction of a variable that is mostly affecting the data, while PC2 is the factor which is the second highest in terms of variance. PCA was performed on the TOFs of ions of $(Al_xGa_{1-x})_2O_3$ with $x = 0.10$–1.0. The TOF for any specific element being constant due to a fixed value of the corresponding mass-to-charge state ratio, the shape of the TOF peaks should retain the similar shape except the peak intensity which would be subjected to change due to the change in the alloy composition. This variation of TOF peaks will not be visible from the TOF spectrum of the entire heterostructure while this peaks shape deviation can be observed when the entire spectrum is sampled equally as shown in Figs. 9(a)–9(k). The
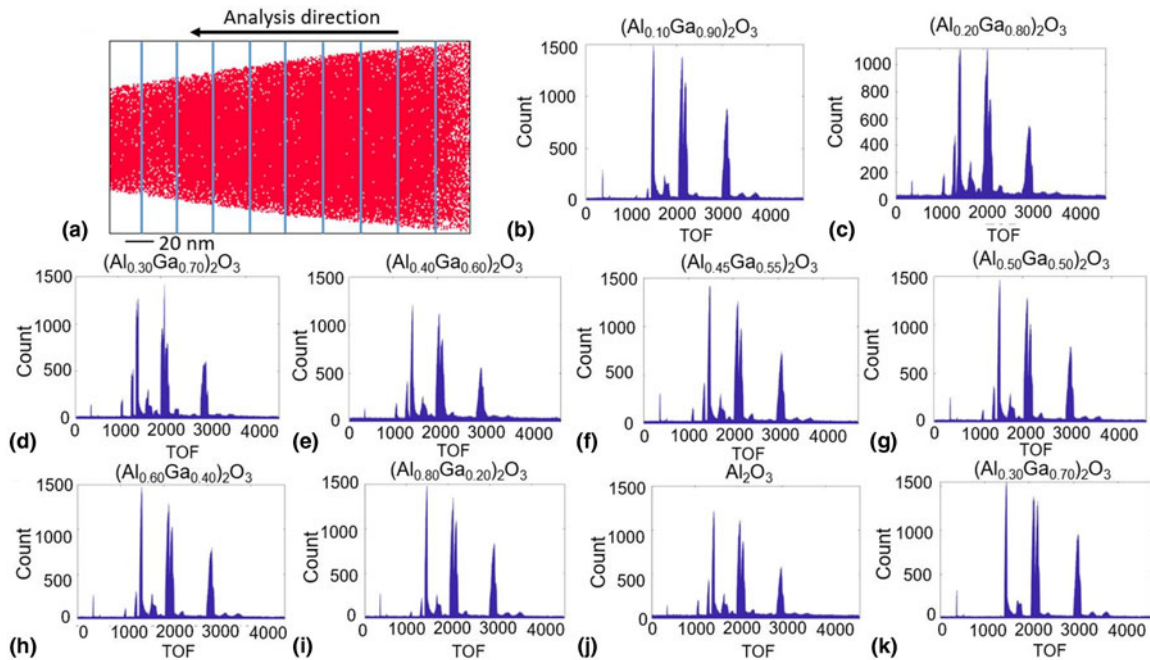
Figure 9: (a–k) Equal sampling of the TOF spectrum for the $(Al_xGa_{1-x})_2O_3$ films with $x = 0.10$–1.0 by sectioning into equal volumes. The typical output of APT is an image showing atom positions having a single TOF spectrum for the whole data set. The first step is to divide the sample into multiple sections, and each section will have a respective TOF spectrum as shown in (b–k). Reprinted from Ref. [29] with the permission of AIP Publishing.
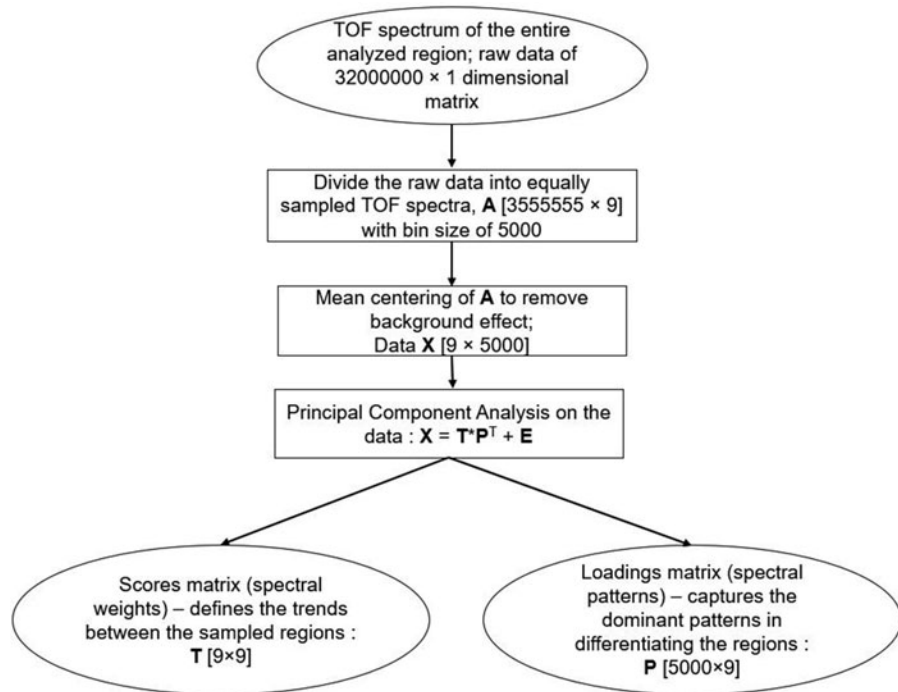
Figure 10: The flow chart illustrating the algorithm used to perform PCA on the TOF of $(Al_xGa_{1-x})_2O_3$ films with $x = 0.1$–1.0. Reprinted from Ref. [29] with the permission of AIP Publishing.

differences in TOF peak shapes and intensities of one sampled spectrum compared with next or previously sampled spectra are arising from the change in the alloy composition. These equally sampled spectra were provided as input to the PCA to extract hidden patterns in these peak deviations to explore phase-related information. The initial processing of the APT TOF data and the algorithm used for the data dimensionality reduction using PCA are described by the flowchart as shown in Fig. 10. Figure 11 shows the PCA result where PC1 is capturing the change in alloy chemistry (Al/Ga ratio) along with the growth which is the largest factor affecting the data, while PC2 is reflecting the TOF peak changes, which is the second most influential factor. From the PC1 versus PC2, a linearly increasing trend up to $x \leq 0.30$ is observed, this positive correlation between the variation of alloy composition and peak shapes. This increasing trend was attributed to degrading crystallinity. Positive correlation up to $x \leq 0.30$ in PC1 versus PC2 suggests that up until this alloy composition, $(Al_xGa_{1-x})_2O_3$, the single-phase crystalline structure is retained. As mentioned earlier, within this Al composition range, the $(Al_xGa_{1-x})_2O_3$ films are β-phase stable. When $x \geq 0.30$ and $x \leq 0.50$, no trend is observed within Al/Ga ratio and TOF peak changes indicating PC1 and PC2 are negatively correlated. This suggests that the presence of a degraded crystallinity within this Al content range. When Al content, $x > 0.50$, a linearly decreasing trend is observed between PC1 and PC2. The retention of this linear trend for $x = 0.60$–1.0 is suggesting that the Al/Ga variation is positively correlated with the TOF peak deviations, while the decreasing value of PC1-PC2 implies the

crystallinity is being restored as Al composition is increasing. This result indicates a new crystalline phase formed. From the XRD result, in this Al content range ($x = 0.6$–1.0), the $(Al_xGa_{1-x})_2O_3$ films are γ-phase stable. Thus, combining APT with the data mining strategy, phase transformation is determined without any supporting tool like STEM or nanodiffraction. This study demonstrates that the capability of APT can be extended to investigate not only the structural chemistry of materials but also information about phase transformation can be obtained.
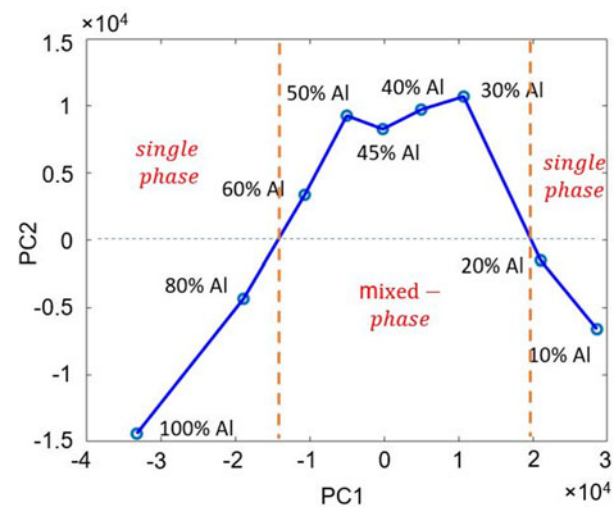

Figure 11: PCA showing phase transition in $(Al_xGa_{1-x})_2O_3$ with $x = 0.10$–1. Reprinted from Ref. [29] with the permission of AIP Publishing.

Doping interaction in $(Al_xGa_{1-x})_2O_3$ by APT

Dopant detection and dopant profile analysis

Extrinsic n-type doping is required to achieve high conductivity in $(Al_xGa_{1-x})_2O_3$ since the intrinsic oxygen vacancies do not contribute in conduction [35, 37]. To realize desired conductivity, it is critical to address the issue with donor compensation [39, 40, 41, 42, 43, 44] that leads to a low carrier mobility at high doping level and adversely affects the electrical and optical properties of the devices [99]. The mechanism of this dopant compensation effect is still under debate. Some studies proposed that n-type dopants involve in the formation of DX transition centers that attributes to the self-compensation of donors [100, 101, 102]. A DX transition center occurs when a donor impurity captures two electrons and undergoes a large lattice relaxation to transform into an acceptor, resulting in fewer electrons available for conduction. Another factor that is accounted for compensating knee is the material defects [99]. The formation of native defects such as cation vacancies (like Ga vacancy, V_{Ga} or Al vacancy, V_{Al}) associated with impurity doping can be electrically favorable and tend to diffuse toward the active bulk region [41]. The interaction of n-type dopants with these native defects (V_{Ga} and V_{Al}) results in the formation of n-type dopant interstitial-III site vacancy defect complexes (V_{Ga}-Si_{Ga} or V_{Al}-Si_{Al} for example) that act as charge trapping centers. This leads to the compensating knee in wide bandgap semiconductors like GaAs, GaN, AlGaN, and Ga_2O_3 [40, 43, 44, 99, 103]. N-type doping is found to be particularly challenging in the wide bandgap alloys when the alloy composition is varied [36]. In $Al_xGa_{1-x}N$, it has been observed that n-type doping at $x > 0.70$ is very challenging because of the drastic increase of dopant activation energy followed by carrier compensation due to deep level defects and deep Si DX centers [104, 105, 106]. In Ge doped AlGaN, dopant atoms are observed to form clusters at high Al content which was attributed to the increase in smaller Al–N bonds compared with larger Ga–N and Ge–N bonds [107]. $(Al_xGa_{1-x})_2O_3$ being a similar class of material system, these above-stated issues may impose difficulties in achieving the desired doping profile. The n-type doping in $(Al_xGa_{1-x})_2O_3$ is theoretically investigated with group IV elements (C, Si, Sn, and Ge) and transition metals (Hf, Zr, and Ta) as they are predicted to substitute on cation sites [36]. Si was found to be the most suitable dopant as it remains a shallow level donor even at the highest Al content while other dopants become deep level donor at high Al. Experimental demonstration of Si doping in $(Al_xGa_{1-x})_2O_3$ is also reported where Si incorporation was confirmed [37, 38, 108, 109], but comprehensive understanding of the atomic-level dopant behavior with the doped $(Al_xGa_{1-x})_2O_3$ films needs further effort. To characterize the n-type doping in $(Al_xGa_{1-x})_2O_3$ with varying Al content, it is extremely important to accurately detect and quantify the dopant elements. Also, a firm knowledge is required about how the dopant atoms are interacting with the matrix, especially, when the alloy composition is varied.

APT has already demonstrated its outstanding capability in characterizing dopants profile in other semiconductor systems having complex 3D geometry and complex alloy chemistry [110, 111, 112]. Inspired from these results, Si doped $(Al_xGa_{1-x})_2O_3$ with $x = 0$–1.0 was investigated by APT [113]. The Si dopant incorporation was confirmed from the APT mass spectrum where Si peaks for both Si^{1+} at 28 Da and Si^{2+} at 14 Da were distinctly identified as shown in Fig. 12. The dopant concentration for Si in each $(Al_xGa_{1-x})_2O_3$ layer was measured and found to be in the range of 1–7×10^{18} cm^{-3}, which was as estimated from the growth ($\sim 5 \times 10^{18}$ cm^{-3}). No peak overlap with the thermal tail from Al^{1+} and Al^{2+} was observed to introduce quantification artifacts, thanks to the optimization of laser pulse energy and base temperature. This implies successful dopant incorporation in each $(Al_xGa_{1-x})_2O_3$ layer regardless of the alloy compositions.

To investigate the dopant distribution whether it is homogeneous or non-homogeneous, statistical FDA from individual alloy composition was performed. Figure 13 reports the FDA of Si distribution from alloy volume of 4 nm thickness, extracted from the bulk of each layer. In all cases, the observed Si distribution closely resembles the binomial fitting with the low value of Pearson coefficient (μ) while a μ value close to 1 would indicate the presence of segregation [94]. The FDA results suggest dopant distribution in each $(Al_xGa_{1-x})_2O_3$ is close to homogeneous and efficient n-type doping was achieved in $(Al_xGa_{1-x})_2O_3$ over the whole alloy composition range.

Dopant interaction in $(Al_xGa_{1-x})_2O_3$

To explore how dopant Si affects the microstructure of the $(Al_xGa_{1-x})_2O_3$ layers with varying alloy composition, the interaction of these dopants with the neighboring atoms of the doped matrix was investigated using radial distribution function (RDF) [114]. RDF is a very efficient statistical analysis technique to examine the affinity between different species located within very short distances [114]. The RDF method was extended to study species interaction with varying alloy compositions. RDF provides the radially outward concentrations starting from each atom of any selected species and returns the probability density of finding an atom j at a distance r given the central atom i [115]. In this case, considering Si as the atom of interest (atom i), the concentration profile of Al and Ga (atom j) starting from each Si atoms in a radially outward direction within small volumes was measured via RDF as illustrated in Fig. 14. RDF determined Ga and Al concentration surrounding each dopant Si atom (considering as the center,
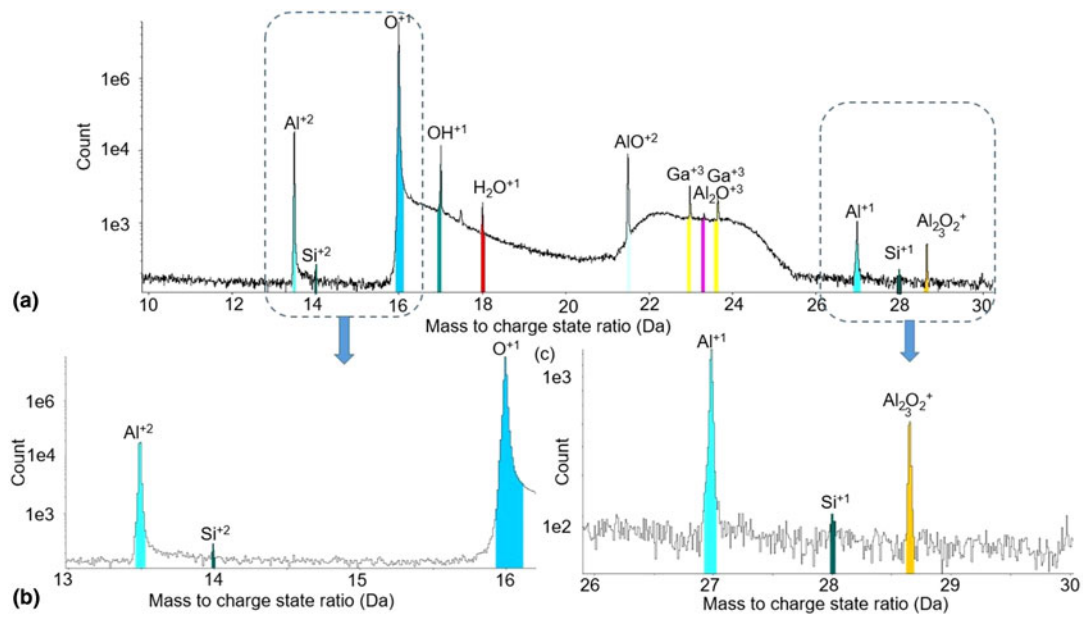
Figure 12: (a) APT mass spectrum (background corrected) of Si doped $(Al_xGa_{1-x})_2O_3$ with $x = 0$–100%; (b) magnified mass spectrum from the dotted region in (a) showing Si peaks at 14 Da associated with Si^{2+} and (c) at 28 Da associated to Si^{1+}. No peak overlap from tails from Al was observed [113].
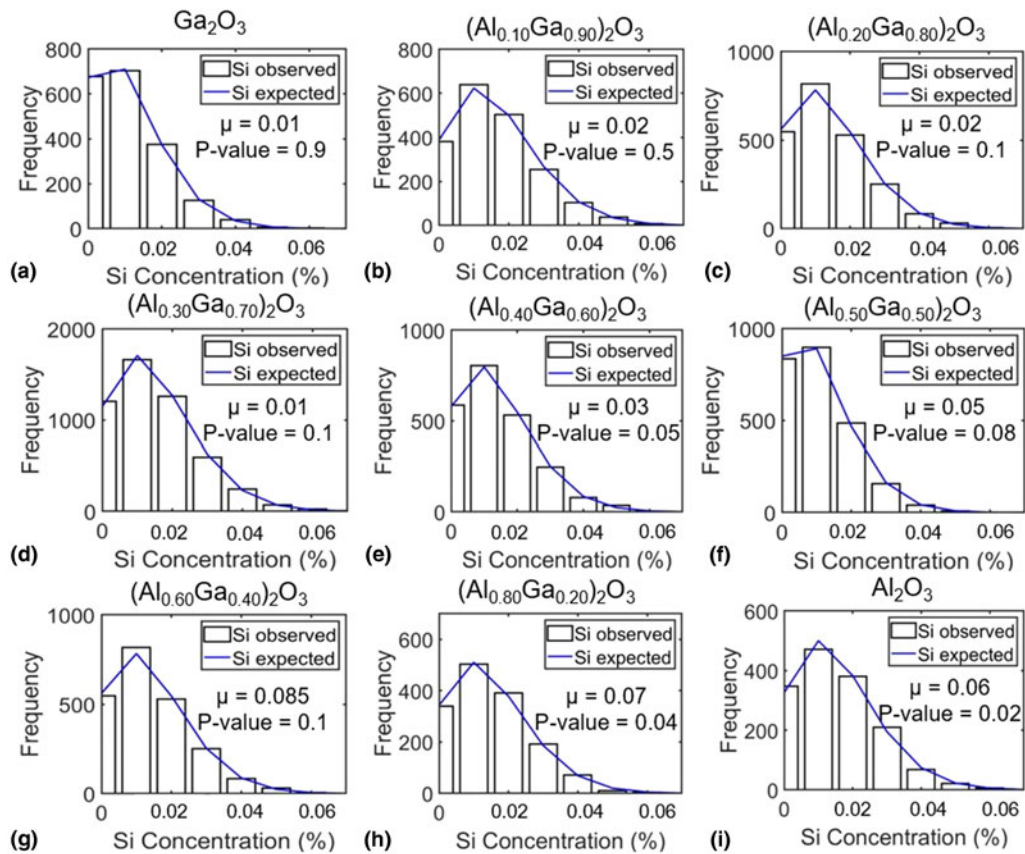
Figure 13: FDA of Si distribution in each layer with Al composition of (b) $x = 0.0$, (c) $x = 0.10$, (d) $x = 0.20$, (e) $x = 0.30$, (f) $x = 0.40$, (g) $x = 0.50$, (h) $x = 0.60$, (i) $x = 0.80$, and (j) $x = 1.0$ [113].
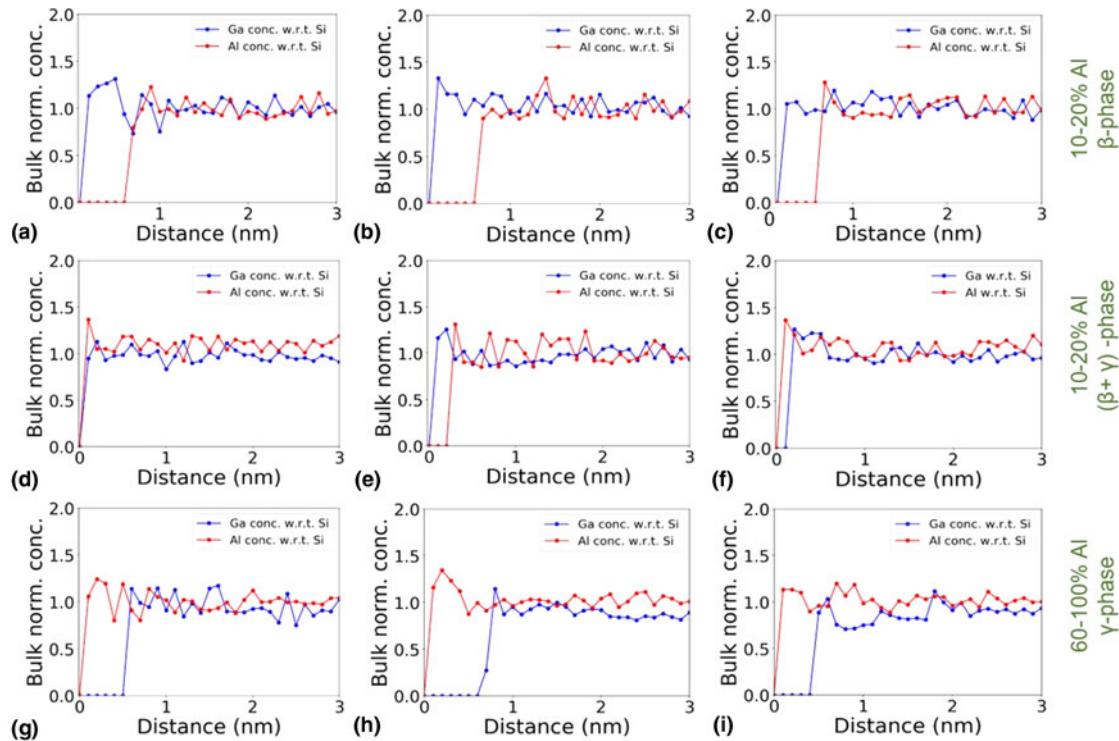
Figure 14: RDF results in each $(Al_xGa_{1-x})_2O_3$ layers showing Si is occupying (a–c) Ga site at $(Al_xGa_{1-x})_2O_3$ at $x = 0.10$–0.20; (d–f) Ga or Al site at $(Al_xGa_{1-x})_2O_3$ at $x = 0.30$–0.50; (g–i) Al site at $(Al_xGa_{1-x})_2O_3$ at $x = 0.60$–0.80 [113].

distance, $d = 0$) within a volume of 10 nm × 10 nm × 1 nm taken in the bulk region of each $(Al_xGa_{1-x})_2O_3$ layer. At low Al contents ($x = 0$–0.20), high Ga concentration surrounding the Si atoms (at $d = 0$) was observed [Figs. 14(a)–14(c)] while low Al concentration suggests, dopant Si is occupying on Ga site. Ga concentration tends to decrease while approaching the location of center Si atoms which suggest the possible presence of Ga vacancy (V_{Ga}). Dopant Si may interact with these V_{Ga} and form V_{Ga}-Si_{Ga} defect complex which contributes to compensating knee [40, 41]. For layers with $x = 0.30$–0.50, the distribution of Ga and Al surrounding the dopant Si is not obvious and Si may substitute in either Ga or Al sites [Figs. 14(d)–14(f)]. This may lead to the formation of V_{Ga}-Si_{Ga} or V_{Al}-Si_{Al} complex. When the Al content is high ($x = 0.60$–1.0), the high Al concentration surrounding the dopants implies Al site occupancy [Figs. 14(g)–14(i)] and the dopant compensation would have dominant V_{Al}-Si_{Al} defect complexes [99]. The information obtained from this analysis was significant in understanding which kind of cationic site n-type dopants would occupy and the type of dominant defects that would be responsible for dopant compensation in $(Al_xGa_{1-x})_2O_3$ when Al content is varied.

Conclusion and outlook

As discussed in this review, the versatile capability of APT to investigate the atomic-scale structural chemistry of

$(Al_xGa_{1-x})_2O_3$ provided unprecedented insight on how phase transformations in this material occur with changing the alloy composition. Complementing APT data with machine learning-based analyses to determine latent features such as phase transformation of $(Al_xGa_{1-x})_2O_3$ can change the paradigm of currently adapted experimental approaches to understand similar phenomena not only for ultra-wide bandgap oxides but also any other materials exhibiting these phase-related issues. The characterization of n-type dopant distribution in $(Al_xGa_{1-x})_2O_3$, as well as, the knowledge of how this dopant influences the doped material when the alloy composition is being varied, revealed information about the dominant type of defect and dopant-defect complex that would affect chemical and physical properties of $(Al_xGa_{1-x})_2O_3$ at different alloy compositions. The structural and compositional information of $(Al_xGa_{1-x})_2O_3$ with varying alloy composition and n-type doping provided in this study would be significant for not only the growth community to grow high-quality material allowing efficient doping but also the device engineers and scientists in designing and fabrication of high-performance devices.

References

1. **J.B. Casady and R.W. Johnson**: Status of silicon carbide (SiC) as a wide-bandgap semiconductor for high-temperature applications: A review. *Solid-State Electron.* **39**, 1409–1422 (1996).

2. **S.J. Pearton, C.R. Abernathy, M.E. Overberg, G. T. Thaler, D.P. Norton, N. Theodoropoulou, A.F. Hebard, Y.D. Park, F. Ren, J. Kim, and L.A. Boatner** *et al.*: Wide band gap ferromagnetic semiconductors and oxides. *J. Appl. Phys.* **93**, 1–13 (2003).

3. **E. Monroy, F. Omnès, and F. Calle**: Wide-bandgap semiconductor ultraviolet photodetectors. *Semicond. Sci. Technol.* **18**, R33–R51 (2003).

4. **S.J. Pearton, C.R. Abernathy, G.T. Thaler, R.M. Frazier, D.P. Norton, F. Ren, Y.D. Park, J.M. Zavada, I. A. Buyanova, W.M. Chen, and A.F. Hebard** *et al.*: Wide bandgap GaN-based semiconductors for spintronics. *J. Phys.: Condens. Matter* **16**, R209–R245 (2004).

5. **M. Razeghi and M. Henini**: Preface. In *Optoelectronic Devices: III Nitrides*, M. Razeghi and M. Henini, eds. (Elsevier, Oxford, 2005); pp. v–vi.

6. **M. Razeghi and M. Henini**: Chapter 1—introduction. In *Optoelectronic Devices: III Nitrides*, M. Razeghi and M. Henini, eds. (Elsevier, Oxford, 2005); pp. 1–8.

7. **S.J. Pearton, F. Ren, M. Tadjer, and J. Kim**: Perspective: Ga_2O_3 for ultra-high power rectifiers and MOSFETS. *J. Appl. Phys.* **124**, 220901 (2018).

8. **J.Y. Tsao, S. Chowdhury, M.A. Hollis, D. Jena, N.M. Johnson, K.A. Jones, R.J. Kaplar, S. Rajan, C.G. Van de Walle, E. Bellotti, C.L. Chua, R. Collazo, M.E. Coltrin, J.A. Cooper, K.R. Evans, S. Graham, T.A. Grotjohn, E.R. Heller, M. Higashiwaki, M.S. Islam, P.W. Juodawlkis, M.A. Khan, A.D. Koehler, J.H. Leach, U.K. Mishra, R.J. Nemanich, R.C.N. Pilawa-Podgurski, J.B. Shealy, Z. Sitar, M.J. Tadjer, A.F. Witulski, M. Wraback, and J.A. Simmons,** *et al.*: Ultrawide-bandgap semiconductors: Research opportunities and challenges. *Adv. Electron. Mater.* **4**, 1600501 (2018).

9. **X. Ma, Y. Zhang, L. Dong, and R. Jia**: First-principles calculations of electronic and optical properties of aluminum-doped $β-Ga_2O_3$ with intrinsic defects. *Results Phys.* **7**, 1582–1589 (2017).

10. **B.W. Krueger, C.S. Dandeneau, E.M. Nelson, S.T. Dunham, F.S. Ohuchi, and M.A. Olmstead**: Variation of band gap and lattice parameters of beta-$(Al_xGa_{1-x})_2O_3$ powder produced by solution combustion synthesis. *J. Am. Ceram. Soc.* **99**, 2467–2473 (2016).

11. **Y.W. Zhang, A. Neal, Z Xia, C. Joishi, J.M. Johnson, Y. Zheng, S. Bajaj, M. Brenner, D. Dorsey, K. Chabak, G. Jessen, J. Hwang, S. Mou, J.P. Heremans, S. Rajan,** *et al.*: Demonstration of high mobility and quantum transport in modulation-doped beta-$(Al_xGa_{1-x})_2O_3/Ga_2O_3$ heterostructures. *Appl. Phys. Lett.* **112**, 173502–173505 (2018).

12. **F.B. Zhang, K. Saito, T. Tanaka, M. Nishio, M. Arita, and Q.X. Guo**: Wide bandgap engineering of $(AlGa)_2O_3$ films. *Appl. Phys. Lett.* **105**, 162107-1–162107-5 (2014).

13. **G.T. Dang, T. Yasuoka, Y. Tagashira, T. Tadokoro, W. Theiss, and T. Kawaharamura**: Bandgap engineering of $α-(Al_xGa_{1-x})_2O_3$ by a mist chemical vapor deposition two-chamber system and verification of Vegard's Law. *Appl. Phys. Lett.* **113**, 062102 (2018).

14. **E. Ahmadi, O.S. Koksaldi, X. Zheng, T. Mates, Y. Oshima, U.K. Mishra, J.S. Speck,** *et al.*: Demonstration of $β-(Al_xGa_{1-x})_2O_3/β-Ga_2O_3$ modulation doped field-effect transistors with Ge as dopant grown via plasma-assisted molecular beam epitaxy. *Appl. Phys. Express* **10**, 071101 (2017).

15. **S. Krishnamoorthy, Z. Xia, C. Joishi, Y. Zhang, J. McGlone, J. Johnson, M. Brenner, A.R. Arehart, J. Hwang, S. Lodha, and S. Rajan,** *et al.*: Modulation-doped $β-(Al_{0.2}Ga_{0.8})_2O_3/Ga_2O_3$ field-effect transistor. *Appl. Phys. Lett.* **111**, 023502 (2017).

16. **Y. Zhang, C. Joishi, Z. Xia, M. Brenner, S. Lodha, and S. Rajan**: Demonstration of $β-(Al_xGa_{1-x})_2O_3/Ga_2O_3$ double heterostructure field effect transistors. *Appl. Phys. Lett.* **112**, 233503 (2018).

17. **E. Ahmadi, Y. Oshima, F. Wu, and J.S. Speck**: Schottky barrier height of Ni to $β-(Al_xGa_{1-x})_2O_3$ with different compositions grown by plasma-assisted molecular beam epitaxy. *Semicond. Sci. Technol.* **32**, 035004 (2017).

18. **A. Vaidya, J. Sarker, Y. Zhang, L. Lubecki, J. Wallace, J.D. Poplawsky, K. Sasaki, A. Kuramata, A. Goyal, J.A. Gardella, B. Mazumder, and U. Singisetti,** *et al.*: Structural, band and electrical characterization of $β-(Al_{0.19}Ga_{0.81})_2O_3$ films grown by molecular beam epitaxy on Sn doped $β-Ga_2O_3$ substrate. *J. Appl. Phys.* **126**, 095702 (2019).

19. **W.Y. Weng, T.J. Hsueh, S.J. Chang, S.C. Hung, G.J. Huang, H.T. Hsueh, Z.D. Huang, C.J. Chiu,** *et al.*: An (AlxGa1-x)2O3 metal-semiconductor-metal VUV photodetector. *IEEE Sens. J.* **11**, 1795–1799 (2011).

20. **S.H. Yuan, C.C. Wang, S.Y. Huang, and D.S. Wuu**: Improved responsivity drop from 250 to 200nm in sputtered gallium oxide photodetectors by incorporating trace aluminum. *IEEE Electron Device Lett.* **39**, 220–223 (2018).

21. **C.C. Wang, S.H. Yuan, S.L. Ou, S.Y. Huang, K.Y. Lin, Y.A. Chen, P.W. Hsiao, and D.S. Wuu,** *et al.*: Growth and characterization of co-sputtered aluminum-gallium oxide thin films on sapphire substrates. *J. Alloys Compd.* **765**, 894–900 (2018).

22. **G.E. Jellison and F.A. Modine**: Erratum: "Parameterization of the optical functions of amorphous materials in the interband region" [Appl. Phys. Lett. 69, 371 (1996)]. *Appl. Phys. Lett.* **69**, 2137–2137 (1996).

23. **H. Ito, K. Kaneko, and S. Fujita**: Growth and band gap control of corundum-structured alpha-$(AlGa)_2O_3$ thin films on sapphire by spray-assisted mist chemical vapor deposition. *Jpn. J. Appl. Phys.* **51**, 100207-1–100207-3 (2012).

24. **T. Uchida, R. Jinno, S. Takemoto, K. Kaneko, and S. Fujita**: Evaluation of band alignment of $α-Ga_2O_3/α-(Al_xGa_1$

$_{-x})_2O_3$ heterostructures by X-ray photoelectron spectroscopy. *Jpn. J. Appl. Phys.* **57**, 040314 (2018).

25. Q. Feng, X. Li, G. Han, L. Huang, F. Li, W. Tang, J. Zhang, and Y. Hao *et al.*: (AlGa)$_2$O$_3$ solar-blind photodetectors on sapphire with wider bandgap and improved responsivity. *Opt. Mater. Express* **7**, 1240–1248 (2017).

26. C. Kranert, M. Jenderka, J. Lenzner, M. Lorenz, H. von Wenckstern, R. Schmidt-Grund, and M. Grundmann *et al.*: Lattice parameters and Raman-active phonon modes of β-(Al$_x$Ga$_{1-x}$)$_2$O$_3$. *J. Appl. Phys.* **117**, 125703 (2015).

27. R. Wakabayashi, T. Oshima, M. Hattori, K. Sasaki, T. Masui, A. Kuramata, S. Yamakoshi, K. Yoshimatsu, and A. Ohtomo *et al.*: Oxygen-radical-assisted pulsed-laser deposition of β-Ga$_2$O$_3$ and β-(Al$_x$Ga$_{1-x}$)$_2$O$_3$ films. *J. Cryst. Growth* **424**, 77–79 (2015).

28. A.F.M.A.U. Bhuiyan, Z. Feng, J.M. Johnson, H.L. Huang, J. Sarker, M. Zhu, M.R. Karim, B. Mazumder, J. Hwang, and H. Zhao *et al.*: Phase transformation in MOCVD growth of (Al$_x$Ga$_{1-x}$)$_2$O$_3$ thin films. *APL Mater.* **8**, 031104 (2020).

29. J. Sarker, S. Broderick, A.F.M.A.U. Bhuiyan, Z. Feng, H. Zhao, and B. Mazumder: A combined approach of atom probe tomography and unsupervised machine learning to understand phase transformation in (Al$_x$Ga$_{1-x}$)$_2$O$_3$. *Appl. Phys. Lett.* **116**, 152101 (2020).

30. T. Oshima, T. Okuno, N. Arai, Y. Kobayashi, and S. Fujita: Beta-Al$_{2x}$Ga$_{2-2x}$O$_3$ thin film growth by molecular beam epitaxy. *Jpn. J. Appl. Phys.* **48** (2009).

31. V.G. Hill, R. Roy, and E.F. Osborn: The system alumina gallia water. *J. Am. Ceram. Soc.* **35**, 135–142 (1952).

32. Y. Zhang, A. Mauze, and J.S. Speck: *Development of Beta-(Al$_x$Ga$_{1-x}$)$_2$O$_3$/Ga$_2$O$_3$ Heterostructures* (University of California Santa Barbara, Santa Barbara, CA, USA, 2019).

33. S.W. Kaun, F. Wu, and J.S. Speck: Beta-(Al$_x$Ga$_{1-x}$)$_2$O$_3$/Ga$_2$O$_3$ (010) heterostructures grown on beta-Ga$_2$O$_3$ (010) substrates by plasma-assisted molecular beam epitaxy. *J. Vac. Sci. Technol., A* **33**, 041508-1– 041508-9 (2015).

34. R. Miller, F. Alema, and A. Osinsky: Epitaxial β-Ga$_2$O$_3$ and β-(Al$_x$Ga$_{1-x}$)$_2$O$_3$/β-Ga$_2$O$_3$ heterostructures growth for power electronics. *IEEE Trans. Semicond. Manuf.* **31**, 467–474 (2018).

35. L. Dong, R. Jia, B. Xin, B. Peng, and Y. Zhang: Effects of oxygen vacancies on the structural and optical properties of β-Ga$_2$O$_3$. *Sci. Rep.* **7**, 1–12 (2017).

36. J.B. Varley, A. Perron, V. Lordi, D. Wickramaratne, and J.L. Lyons: Prospects for n-type doping of (Al$_x$Ga$_{1-x}$)$_2$O$_3$ alloys. *Appl. Phys. Lett.* **116**, 172104 (2020).

37. A. Hassa, H.v. Wenckstern, L. Vines, and M. Grundmann: Influence of oxygen pressure on growth of Si-doped β-(Al$_x$Ga$_{1-x}$)$_2$O$_3$ thin films on c-sapphire substrates by pulsed laser deposition. *ECS J. Solid State Sci. Technol.* **8**, Q3217–Q3220 (2019).

38. A.F.M. Anhar Uddin Bhuiyan, Z. Feng, J.M. Johnson, Z. Chen, H.L. Huang, J. Hwang, and H. Zhao, *et al.*: MOCVD epitaxy of β-(Al$_x$Ga$_{1-x}$)$_2$O$_3$ thin films on (010) Ga$_2$O$_3$ substrates and N-type doping. *Appl. Phys. Lett.* **115**, 120602 (2019).

39. W. Götz, N. Johnson, C. Chen, H. Liu, C. Kuo, and W. Imler: Activation energies of Si donors in GaN. *Appl. Phys. Lett.* **68**, 3144–3146 (1996).

40. A. Uedono, K. Tenjinbayashi, T. Tsutsui, Y. Shimahara, H. Miyake, K. Hiramatsu, N. Oshima, R. Suzuki, and S. Ishibashi *et al.*: Native cation vacancies in Si-doped AlGaN studied by monoenergetic positron beams. *J. Appl. Phys.* **111**, 013512 (2012).

41. S.F. Chichibu, H. Miyake, Y. Ishikawa, M. Tashiro, T. Ohtomo, K. Furusawa, K. Hazu, K. Hiramatsu, and A. Uedono *et al.*: Impacts of Si-doping and resultant cation vacancy formation on the luminescence dynamics for the near-band-edge emission of Al$_{0.6}$Ga$_{0.4}$N films grown on AlN templates by metalorganic vapor phase epitaxy. *J. Appl. Phys.* **113**, 213506 (2013).

42. D. Gogova, G. Wagner, M. Baldini, M. Schmidbauer, K. Irmscher, R. Schewski, Z. Galazka, M. Albrecht, and R. Fornari *et al.*: Structural properties of Si-doped β-Ga$_2$O$_3$ layers grown by MOVPE. *J. Cryst. Growth* **401**, 665–669 (2014).

43. Z. Zhang, E. Farzana, A. Arehart, and S.A. Ringel: Deep level defects throughout the bandgap of (010) β-Ga$_2$O$_3$ detected by optically and thermally stimulated defect spectroscopy. *Appl. Phys. Lett.* **108**, 052105 (2016).

44. S. Chichibu, A. Iwai, Y. Nakahara, S. Matsumoto, H. Higuchi, L. Wei, and S. Tanigawa *et al.*: Monoenergetic positron beam study of Si-doped GaAs epilayers grown by low-pressure metalorganic chemical vapor deposition using tertiarybutylarsine. *J. Appl. Phys.* **73**, 3880–3885 (1993).

45. M.A. Khan, S.P. Ringer, and R. Zheng: Atom probe tomography on semiconductor devices. *Adv. Mater. Interfaces* **3**, 1500713 (2016).

46. S.M. Davidson: Semiconductor material assessment by scanning electron microscopy. *J. Microsc.* **110**, 177–204 (1977).

47. X. Wei, L. Zhao, J. Wang, Y. Zeng, and J. Li: Characterization of nitride-based LED materials and devices using TOF-SIMS. *Surf. Interface Anal.* **46**, 299–302 (2014).

48. M. Bosman, Y. Zhang, C.K. Cheng, X. Li, X. Wu, X.L. Pey, C.T. Lin, Y.W. Chen, S.H. Hsu, and C.H. Hsu *et al.*: The distribution of chemical elements in Al- or La-capped high-κ metal gate stacks. *Appl. Phys. Lett.* **97**, 103504 (2010).

49. N. Nakagiri, T. Yamamoto, H. Sugimura, Y. Suzuki, M. Miyashita, and S. Watanabe: Application of scanning capacitance microscopy to semiconductor devices. *Nanotechnology* **8**, A32–A37 (1997).

50. M. Grasserbauer and G. Stingeder: Surface analysis of semi-conductors with SIMS. *TrAC, Trends Anal. Chem.* **3**, 133–139 (1984).

51. T.F. Kelly, D.J. Larson, K. Thompson, R.L. Alvis, J.H. Bunton, J.D. Olson, and B.P. Gorman *et al.*: Atom probe tomography of electronic materials. *Annu. Rev. Mater. Res.* **37**, 681–727 (2007).

52. O.G. Licata and B. Mazumder: Application of atom probe tomography for advancing GaN based technology. *Int. J. High Speed Electron. Syst.* **28**, 1940005 (2019).

53. A.A. Gribb and T. Kelly: Atom probe analysis. *Adv. Mater. Process.* **162**, 31–34 (2004).

54. B. Gault, M.P. Moody, J.M. Cairney, and S.P.J.M.T. Ringer: Atom probe crystallography. *Mater. Today* **15**, 378–386 (2012).

55. M. Miller and E.J.M. Kenik: Atom probe tomography: A technique for nanoscale characterization. *Microsc. Microanal.* **10**, 336–341 (2004).

56. T.F. Kelly and M. Miller: Atom probe tomography. *Rev. Sci. Instrum.* **78**, 031101 (2007).

57. D.J. Larson, T. Prosa, R.M. Ulfig, B.P. Geiser, and T.F. Kelly: *Local Electrode Atom Probe Tomography* (Springer Science, New York, United States, 2013).

58. B. Mazumder, M.H. Wong, C.A. Hurni, J.Y. Zhang, U.K. Mishra, and J.S. Speck: Asymmetric interfacial abruptness in N-polar and Ga-polar GaN/AlN/GaN heterostructures. *Appl. Phys. Lett.* **101**, 091601 (2012).

59. B. Mazumder, X. Liu, R. Yeluri, F. Wu, U.K. Mishra, and J.S. Speck: Atom probe tomography studies of Al_2O_3 gate dielectrics on GaN. *J. Appl. Phys.* **116**, 134101 (2014).

60. S.W. Kaun, B. Mazumder, M.N. Fireman, E.C.H. Kyle, U.K. Mishra, and J.S. Speck: Pure AlN layers in metal-polar AlGaN/AlN/GaN and AlN/GaN heterostructures grown by low-temperature ammonia-based molecular beam epitaxy. *Semicond. Sci. Technol.* **30**, 055010 (2015).

61. H. Li, B. Mazumder, B. Bonef, S. Keller, S. Wienecke, J.S. Speck, S.P. Denbaars, and U.K. Mishra *et al.*: Characterization of N-polar AlN in GaN/AlN/(Al,Ga)N hetero-structures grown by metal-organic chemical vapor deposition. *Semicond. Sci. Technol.* **32**, 115004 (2017).

62. J.E. Schmidt, L. Peng, A.L. Paioni, H.L. Ehren, W. Guo, B. Mazumder, D.A.M. de Winter, Ö Attila, D. Fu, A.D. Chowdhury, K. Houben, M. Baldus, J.D. Poplawsky, and B.M. Weckhuysen *et al.*: Isolating clusters of light elements in molecular sieves with atom probe tomography. *J. Am. Chem. Soc.* **140**, 9154–9158 (2018).

63. R. Emma, I. Mahaboob, K. Hogan, S. Tozier, V. Meyers, B. McEwen, S. Novak, B. Mazumder, L.D. Bell, and F.S. Shahedipour-Sandvik, *et al.*: Enhanced p-type conductivity in N-polar GaN photocathode structures and correlation with

GaN hillock density (Conference Presentation) .In *Proceedings of SPIE (March 13).* (**Vol. 10918**, San Francisco, California, US, 2019).

64. M.R. Karim, B.H.D. Jayatunga, M. Zhu, R.A. Lalk, O. Licata, B. Mazumder, J. Hwang, K. Kash, and H. Zhao *et al.*: Effects of cation stoichiometry on surface morphology and crystallinity of $ZnGeN_2$ films grown on GaN by metalorganic chemical vapor deposition. *AIP Adv.* **10**, 065302 (2020).

65. E. Rocco, O. Licata, I. Mahaboob, K. Hogan, S. Tozier, V. Meyers, B. McEwen, S. Novak, B. Mazumder, M. Reshchikov, L.D. Bell, and F. Shahedipour-Sandvik *et al.*: Hillock assisted p-type enhancement in N-polar GaN:Mg films grown by MOCVD. *Sci. Rep.* **10**, 1426 (2020).

66. B. Mazumder, A. Vella, and B.J.U. Déconihout: Evaporation mechanisms of MgO in laser assisted atom probe tomography. *Ultramicroscopy* **111**, 571–575 (2011).

67. N. Dawahre, G. Shen, S. Balci, W. Baughman, D.S. Wilbert, N. Harris, L. Butler, R. Martens, S.M. Kim, and P. Kung *et al.*: Atom probe tomography of zinc oxide nanowires. *J. Electron. Mater.* **41**, 801–808 (2012).

68. B. Mazumder, S.W. Kaun, J. Lu, S. Keller, U.K. Mishra, and J.S.J.A.P.L. Speck: Atom probe analysis of AlN interlayers in AlGaN/AlN/GaN heterostructures. *Appl. Phys. Lett.* **102**, 111603 (2013).

69. L. Mancini, N. Amirifar, D. Shinde, I. Blum, M. Gilbert, A. Vella, F. Vurpillot, W. Lefebvre, R. Lardé, E. Talbot, P. Pareige, X. Portier, A. Ziani, C. Davesnne, C. Durand, J. Eymery, R. Butté, J.F. Carlin, N. Grandjean, and L. Rigutti *et al.*: Composition of wide bandgap semiconductor materials and nanostructures measured by atom probe tomography and its dependence on the surface electric field. *J. Phys. Chem. C* **118**, 24136–24151 (2014).

70. S. Madireddy, D.W. Chung, T. Loeffler, S.K.R.S. Sankaranarayanan, D.N. Seidman, P. Balaprakash, and O. Heinonen *et al.*: Phase segmentation in atom-probe tomography using deep learning-based edge detection. *Sci. Rep.* **9**, 1–10 (2019).

71. S.R. Broderick, A. Bryden, S.K. Suram, and K. Rajan: Data mining for isotope discrimination in atom probe tomography. *Ultramicroscopy* **132**, 121–128 (2013).

72. Y. Wei, B. Gault, R.S. Varanasi, D. Raabe, M. Herbig, and A.J. Breen: Machine-learning-based atom probe crystallographic analysis. *Ultramicroscopy* **194**, 15–24 (2018).

73. A. Mukherjee, S. Broderick, and K. Rajan: Modularity optimization for enhancing edge detection in microstructural features using 3D atomic chemical scale imaging. *J. Vac. Sci. Technol., A* **38**, 033207 (2020).

74. R.A.D. Mackenzie, A. Cerezo, and G.D.W. Smith: Characterization of nanometer-scale compositional variations

using field ion microscopy and the position sensitive atom probe. *Nanostruct. Mater.* **3**, 203–210 (1993).

75. D.J. Larson, P.P. Camus, J.L. Vargas, T.F. Kelly, and M.K. Miller: Specimen preparation and atom probe field ion microscopy of BSCCO-2212 superconductors. *J. Phys. IV* **06**, C5-271–C5-276 (1996).

76. T. Philippe, F.D. Geuser, S. Duguay, W. Lefebvre, O. Cojocaru-Mirédin, G.D. Costa, andD. Blavette *et al.*: Clustering and nearest neighbour distances in atom-probe tomography. *Ultramicroscopy* **109**, 1304–1309 (2009).

77. B. Gault, D. Haley, F. de Geuser, M.P. Moody, E.A. Marquis, D.J. Larson, andB.P. Geiser *et al.*: Advances in the reconstruction of atom probe tomography data. *Ultramicroscopy* **111**, 448–457 (2011).

78. T.T. Tsong: *Atom-Probe Field Ion Microscopy: Field Ion Emission, and Surfaces and Interfaces at Atomic Resolution* (Cambridge University Press, New York, US, 2005).

79. K. Thompson, D. Lawrence, D. Larson, J. Olson, T. Kelly, and B.J.U. Gorman: In situ site-specific specimen preparation for atom probe tomography. *Ultramicroscopy* **107**, 131–139 (2007).

80. T.F. Kelly and D.J. Larson: Atom probe tomography 2012. *Annu. Rev. Mater. Res.* **42**, 1–31 (2012).

81. K.E. Yoon, D.N. Seidman, C. Antoine, and P. Bauer: Atomic-scale chemical analyses of niobium oxide/niobium interfaces via atom-probe tomography. *Appl. Phys. Lett.* **93**, 132502 (2008).

82. R. Rachbauer, S. Massl, E. Stergar, P. Felfer, and P.H. Mayrhofer: Atom probe specimen preparation and 3D interfacial study of Ti–Al–N thin films. *Surf. Coat. Technol.* **204**, 1811–1816 (2010).

83. D. Larson, A. Petford-Long, A. Cerezo, G. Smith, D. Foord, and T.J.A.p.l. Anthony: Three-dimensional atom probe field-ion microscopy observation of Cu/Co multilayer film structures. *Appl. Phys. Lett.* **73**, 1125–1127 (1998).

84. D.J. Larson, A. Cerezo, J. Juraszek, K. Hono, and G.J.M.b. Schmitz: Atom-probe tomographic studies of thin films and multilayers. *MRS Bull.* **34**, 732–737 (2009).

85. T.F. Kelly, and D.J. Larson *et al.*: Atom probe tomography 2012. *Annu. Rev. Mater. Res.* **42**, 1–31 (2012).

86. Z. Peng, F. Vurpillot, P.-P. Choi, Y. Li, D. Raabe, and B. Gault: On the detection of multiple events in atom probe tomography. *Ultramicroscopy* **189**, 54–60 (2018).

87. B. Mazumder, J. Sarker, Y. Zhang, J.M. Johnson, M. Zhu, S. Rajan, andJ. Hwang *et al.*: Atomic scale investigation of chemical heterogeneity in β-(Al$_x$Ga$_{1-x}$)$_2$O$_3$ films using atom probe tomography. *Appl. Phys. Lett.* **115**, 132105 (2019).

88. J. Sarker, Y. Zhang, M. Zhu, S. Rajan, J. Hwang, and B. Mazumder: Understanding the growth mechanism of β-(Al$_x$Ga$_{1-x}$)$_2$O$_3$ by atom probe tomography. *Microsc. Microanal.* **25**, 2508–2509 (2019).

89. B. Gault, M.P. Moody, J.M. Cairney, and S.P. Ringer: *Atom Probe Microscopy* (Springer Science & Business Media, New York, US, 2012).

90. T. Frolov, M. Asta, and Y.J.P.R.B. Mishin: Segregation-induced phase transformations in grain boundaries. *Phys. Rev. B* **92**, 020103 (2015).

91. C. Kumara, A.R. Balachandramurthi, S. Goel, F. Hanning, and J. Moverare: Toward a better understanding of phase transformations in additive manufacturing of alloy 718. *Materialia* **13**, 100862 (2020).

92. W. Guo, D.A. Garfinkel, J.D. Tucker, D. Haley, G.A. Young, and J.D. Poplawsky: An atom probe perspective on phase separation and precipitation in duplex stainless steels. *Nanotechnology* **27**, 254004 (2016).

93. A. Shariq and N. Mattern: A study of phase separated Ni66Nb17Y17 metallic glass using atom probe tomography. *Ultramicroscopy* **111**, 1370–1374 (2011).

94. A. Devaraj, M. Gu, R. Colby, P. Yan, C.M. Wang, J.M. Zheng, J. Xiao, A. Genc, J.G. Zhang, I. Belharouak, D. Wang, K. Amine, and S. Thevuthasan *et al.*: Visualizing nanoscale 3D compositional fluctuation of lithium in advanced lithium-ion battery cathodes. *Nat. Commun.* **6**, 8014 (2015).

95. P. Vogt, A. Mauze, F. Wu, B. Bonef, and J.S. Speck: Metal-oxide catalyzed epitaxy (MOCATAXY): The example of the O plasma-assisted molecular beam epitaxy of β-(Al$_x$Ga$_{1-x}$)$_2$O$_3$/β-Ga$_2$O$_3$ heterostructures. *Appl. Phys. Express* **11**, 115503 (2018).

96. J. Li, X. Chen, T. Ma, X. Cui, F.F. Ren, S. Gu, R. Zhang, Y. Zheng, S.P. Ringer, L. Fu, H.H. Tan, C. Jagadish, andJ. Ye *et al.*: Identification and modulation of electronic band structures of single-phase beta-(Al$_x$Ga$_{1-x}$)$_2$O$_3$ alloys grown by laser molecular beam epitaxy. *Appl. Phys. Lett.* **113**, 041901 (2018).

97. Z. Peng, Y. Lu, C. Hatzoglou, and A.K. da Silva *et al.*: An automated computational approach for complete in-plane compositional interface analysis by atom probe tomography. *Microsc. Microanal.* **25**, 389–400 (2019).

98. E. Mejía-Uriarte, R. Sato-Berru, M. Navarrete, O. Kolokoltsev, and J.M. Saniger: Determination of phase transition by principal component analysis applied to Raman spectra of polycristalline BATIO$_3$ at low and high temperature. *J. Appl. Res. Technol.* **10**, 57–62 (2012).

99. J.S. Harris, J.N. Baker, B.E. Gaddy, I. Bryan, Z. Bryan, K.J. Mirrielees, P. Reddy, R. Collazo, Z. Sitar, and D.L. Irving *et al.*: On compensation in Si-doped AlN. *Appl. Phys. Lett.* **112**, 152101 (2018).

100. C. Park and D.J.P.R.B. Chadi: Stability of deep donor and acceptor centers in GaN, AlN, and BN. *Phys. Rev. B* **55**, 12995 (1997).

101. M. McCluskey, N. Johnson, C.G. Van de Walle, D. Bour, M. Kneissl, and W.J.P.R.L. Walukiewicz: Metastability of oxygen donors in AlGaN. *Phys. Rev. Lett.* **80**, 4008 (1998).

102. L. Gordon, J.L. Lyons, A. Janotti, and C.G. Van de Walle: Hybrid functional calculations of DX centers in AlN and GaN. *Phys. Rev. B* **89**, 085204 (2014).

103. E. Farzana, E. Ahmadi, J.S. Speck, A.R. Arehart, and S.A. Ringel: Deep level defects in Ge-doped (010) β-Ga$_2$O$_3$ layers grown by plasma-assisted molecular beam epitaxy. *J. Appl. Phys.* **123**, 161410 (2018).

104. M.L. Nakarmi, K.H. Kim, K. Zhu, J.Y. Lin, and H.X. Jiang: Transport properties of highly conductive n-type Al-rich Al$_x$Ga$_{1-x}$N($x \geqslant 0.7$). *Appl. Phys. Lett.* **85**, 3769–3771 (2004).

105. B. Borisov, V. Kuryatkov, Y. Kudryavtsev, R. Asomoza, S. Nikishin, D.Y. Song, M. Holtz, and H. Temkin*et al.*: Si-doped Al$_x$Ga$_{1-x}$N($0.56 \leqslant x \leqslant 1$) layers grown by molecular beam epitaxy with ammonia. *Appl. Phys. Lett.* **87**, 132106 (2005).

106. R. Collazo, S. Mita, J. Xie, A. Rice, J. Tweedie, R. Dalmau, and Z. Sitar*et al.*: Progress on n-type doping of AlGaN alloys on AlN single crystal substrates for UV optoelectronic applications. *Phys. Status Solidi C* **8**, 2031–2033 (2011).

107. R. Blasco, A. Ajay, E. Robin, C. Bougerol, K. Lorentz, L.C. Alves, I. Mouton, L. Amichi, A. Grenier, and E. Monroy*et al.*: Electrical and optical properties of heavily Ge-doped AlGaN. *J. Phys. D: Appl. Phys.* **52**, 125101 (2019).

108. P. Ranga, A. Rishinaramangalam, J. Varley, A. Bhattacharyya, D. Feezell, and S. Krishnamoorthy: Si-doped β-(Al$_{0.26}$Ga$_{0.74}$)$_2$O$_3$ thin films and heterostructures grown by metalorganic vapor-phase epitaxy. *Appl. Phys. Express* **12**, 111004 (2019).

109. P. Ranga, A. Bhattacharyya, A. Rishinaramangalam, Y.K. Ooi, M.A. Scarpulla, D. Feezell, and S. Krishnamoorthy*et al.*: Delta-doped β-Ga$_2$O$_3$ thin films and β-(Al$_{0.26}$Ga$_{0.74}$)$_2$O$_3$/β-Ga$_2$O$_3$ heterostructures grown by metalorganic vapor-phase epitaxy. *Appl. Phys. Express* **13**, 045501 (2020).

110. P.A. Ronsheim, M. Hatzistergos, and S. Jin: Dopant measurements in semiconductors with atom probe tomography. *J. Vac. Sci. Technol., B* **28**, C1E1–C1E4 (2010).

111. S. Du, T. Burgess, B. Gault, Q. Gao, P. Bao, L. Li, X. Cui, W.K. Yeoh, H. Liu, L. Yao, A.V. Ceguerra, H.H. Tan, C. Jagadish, S.P. Ringer, and R. Zheng*et al.*: Quantitative dopant distributions in GaAs nanowires using atom probe tomography. *Ultramicroscopy* **132**, 186–192 (2013).

112. W.K. Yeoh, S.-W. Hung, S.-C. Chen, Y.-H. Lin, and J.J. Lee: Quantification of dopant species using atom probe tomography for semiconductor application. *Surf. Interface Anal.* **52**, 318–323 (2020).

113. J. Sarker, A. F. M. A. U. Bhuiyan, Z. Feng, H. Zhao, and B. Mazumder, Direct observation of site-specific dopant substitution in Si doped (Al$_x$Ga$_{1-x}$)$_2$O$_3$ via atom probe tomography, http://arxiv.org/abs/2009.01390, Journal Unpublished 2020.

114. J.E. Schmidt, L. Peng, J.D. Poplawsky, and B.M.J.A.C.I.E. Weckhuysen: Nanoscale chemical imaging of zeolites using atom probe tomography. *Angew. Chem., Int. Ed.* **57**, 10422–10435 (2018).

115. J. Zhou, J. Odqvist, M. Thuvander, and P. Hedström: Quantitative evaluation of spinodal decomposition in Fe-Cr by atom probe tomography and radial distribution function analysis. *Microsc. Microanal.* **19**, 665–675 (2013).